Cellular Interactome Dynamics during Paclitaxel Treatment

Juan D. Chavez[1], **Andrew Keller**[1], **Bo Zhou**[2,3,4], **Rong Tian**[2,3,4], **James E. Bruce**[1,5,*]

[1]Department of Genome Sciences, University of Washington, Seattle, WA 98105, USA

[2]Department of Bioengineering, University of Washington, Seattle, WA 98105, USA

[3]Department of Anesthesiology and Pain Medicine, University of Washington, Seattle, WA 98105, USA

[4]Mitochondria and Metabolism Center, University of Washington, Seattle, WA 98105, USA

[5]Lead Contact

SUMMARY

Cell-cycle inhibitors, including paclitaxel, are among the most widely used and effective cancer therapies. However, several challenges limit the success of paclitaxel, including drug resistance and toxic side effects. Paclitaxel is thought to act primarily by stabilizing microtubules, locking cells in a mitotic state. However, the resulting cytotoxicity and tumor shrinkage rates observed cannot be fully explained by this mechanism alone. Here we apply quantitative chemical cross-linking with mass spectrometry analysis to paclitaxel-treated cells. Our results provide large-scale measurements of relative protein levels and, perhaps more importantly, changes to protein conformations and interactions that occur upon paclitaxel treatment. Drug concentration-dependent changes are revealed in known drug targets including tubulins, as well as many other proteins and protein complexes involved in apoptotic signaling and cellular homeostasis. As such, this study provides insight into systems-level changes to protein structures and interactions that occur with paclitaxel treatment.

In Brief

Chavez et al. reveal interactome changes in cells treated with mitotic inhibitors using quantitative cross-linking and mass spectrometry. Cross-links reflect interaction/conformational changes specific for drug type and concentration, which are not evident by protein expression levels. Microtubule stabilization, cytoskeletal alteration, and changes to mitochondrial function are visualized in cross-link levels.

*Correspondence: jimbruce@uw.edu.

Graphical Abstract
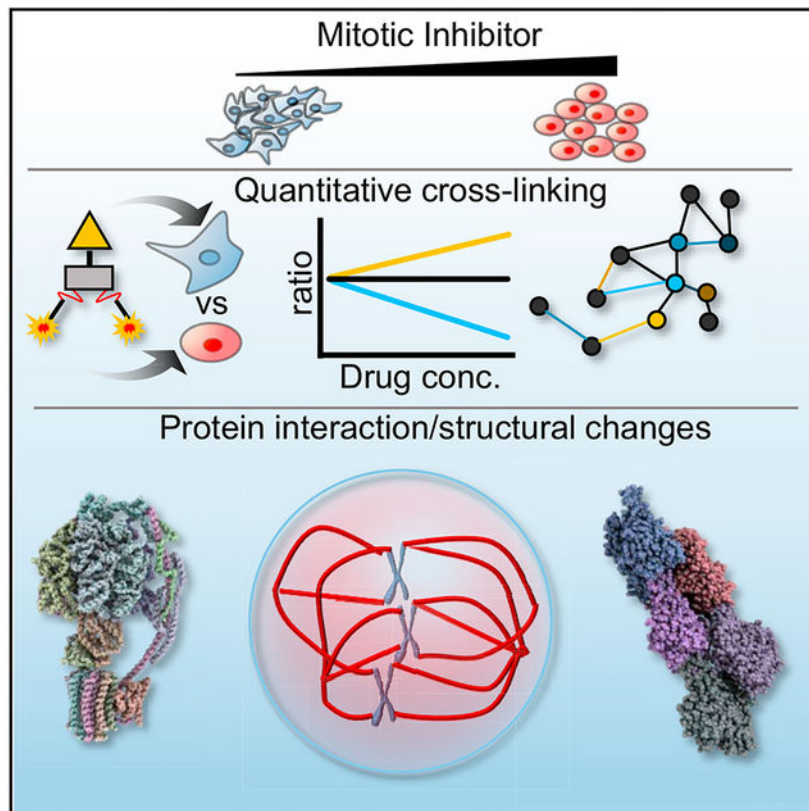
INTRODUCTION

Unregulated cell growth due to cell-cycle dysfunction is a hallmark of cancer. Drugs that target cell-cycle proteins to inhibit the cell cycle have therefore become useful for cancer treatment. Paclitaxel (PTX, Taxol) is among the profitable and most widely used chemotherapies. The primary mode of action of PTX is inhibition of the cell cycle in M phase, stabilizing microtubules (MTs) by binding directly to β-tubulin and causing cell death as a consequence of mitotic arrest. Despite much evidence supporting the prevailing hypothesis, it has been noted that the cytotoxic PTX effects of mitotic arrest are not sufficient to account for tumor shrinkage rates observed for human tumors with slow doubling times (Komlodi-Pasztor et al., 2011; Mitchison, 2012; Weaver, 2014). A study of PTX cytotoxicity in breast cancer led to an alternative hypothesis that PTX can induce cancer cell death due to missegregation of chromosomes on multipolar spindles (Zasadil et al., 2014). Although the primary drug target and mechanism of action for PTX are known, the broad molecular changes to protein structures and interactions during PTX treatment of cells remain largely unknown, particularly with varying drug concentrations. Insight into the molecular changes occurring during PTX-induced mitotic block would be useful for development of future therapeutics and provide insight into the fundamental changes occurring when cells enter mitosis.

There is a need for new approaches to probe the cellular state of the proteome, including protein structures and interactions. Changes to protein conformations and interactions can affect biological function independent of protein expression or abundance-level changes. Chemical cross-linking with mass spectrometry (XL-MS) has emerged as a technique allowing systems-level structural biology measurements to be made within living cells (Chavez and Bruce, 2019; Chavez et al., 2013; Weisbrod et al., 2013a; Yang et al., 2012; Zhang et al., 2008; Zheng et al., 2011). XL-MS provides information on proximal residues that are reactive to the cross-linker, in this case Lys. Information is gained on the identities of interacting proteins and can be used to aid molecular modeling and docking experiments for structural determination. The use of stable isotope labeling allows quantitative comparisons of cross-linked peptide pair levels (qXL-MS) to be made under various biological states or perturbations (Chen and Rappsilber, 2018). For qXL-MS, isotope labels can be incorporated into proteins, using metabolic labeling, or incorporated into the chemical cross-linker molecule (Zhong et al., 2017). Use of metabolic labeling with stable isotope labeling by amino acids in cell culture (SILAC) (Ong et al., 2002) allows quantitative measurements of cross-linked peptide pairs and non-cross-linked peptides from the same sample, enabling visualization of protein conformational and interaction-level changes, as well as global protein abundance-level changes. Importantly, qXL-MS can detect changes in protein conformations and interactions that may not be reflected by quantitative measurements of global protein abundance levels. Exploiting this feature allowed use of qXL-MS for detection of conformational changes in topoisomerase II (TOP2A), corresponding with increased TOP2A activity despite no change in TOP2A gene expression or protein abundance levels. These interactome changes uniquely revealed TOP2A conformational regulation as at least part of the mechanism of drug resistance in cells with acquired resistance to the topoisomerase I inhibitor SN-38 (Chavez et al., 2015). After demonstrating the ability of qXL-MS to uncover important molecular differences existing between phenotypes (i.e., drug-resistant versus drug-sensitive cancer cells), we explored the use of the technique for the analysis of drug-induced changes. For this purpose, drugs targeting the molecular chaperone heat shock protein 90 (Hsp90) were applied to HeLa cells, and qXL-MS analysis was performed to evaluate protein conformational and interaction-level changes induced by drug treatment (Chavez et al., 2016b). qXL-MS allowed detection of structural changes to the Hsp90 protein machinery that were Hsp90 isoform, as well as specific to drug type (N-terminal domain versus C-terminal domain inhibitor) (Chavez et al., 2016b). Encouraged by these previous studies, we set out to explore the use of qXL-MS to probe the effects of drugs targeting the cell cycle.

Here we apply qXL-MS with SILAC labeling in cultured human cancer cells treated with varying concentrations of PTX to reveal large-scale protein conformational and interaction changes (Figure 1). We compare the PTX results with qXL-MS data from cells treated with mitotic inhibitors with differing mechanisms of action, namely, with S-trityl-L-cysteine (STLC), an inhibitor of the Kinesin-like protein KIF11, and with combretastatin A-4 (CA4) and nocodazole (NOC), both of which inhibit MT polymerization. Our results demonstrate that the expected changes of PTX treatment, including the stabilization of MTs, can be visualized in cells by qXL-MS. Dose-dependent changes to several classes of protein complexes involved in progression of the cell cycle are resolved, providing insight into the

molecular-level changes occurring with PTX treatment. Cross-links in proteins with established roles in apoptosis, including keratins 8 and 18, prohibitins (PHBs), and Hsp90, displayed quantitative changes tracking with PTX concentration. We also demonstrate the effects of PTX on mitochondrial bioenergetics that correspond with cross-link-level changes in key mitochondrial complexes, including ATP synthase. These conformational and interaction changes induced by PTX, STLC, CA4, and NOC provide mechanistic insight into the action of these mitotic inhibitors. The results presented herein also serve as evidence for the general applicability of the qXL-MS methodology, illustrating the ability to distinguish drug-specific changes to protein conformations and interactions.

RESULTS

PTX Treatment of HeLa Cells

HeLa cells were treated with varying concentrations of PTX and analyzed by live cell imaging with a Cytation 5 imaging system. The effect of PTX treatment is clearly visible as cells become locked in mitosis, as shown in Figure 1. Under a range of PTX concentrations (0, 5, 10, 20, 50, 100, and 500 nM) the maximum fraction of cells locked in mitosis was observed at 18 h, approaching 80% under the highest concentration of PTX. This is approximately the doubling time of HeLa cells under the growth conditions used in these experiments. Beyond 18 h, cell death becomes evident, particularly at higher PTX concentrations. To observe the maximal differential effect of PTX on the cells, 18 h was chosen as the treatment time for the quantitative cross-linking experiments. Similarly, a range of concentrations were explored for NOC (300 nM, 1 μM, and 3 μM), CA4 (0.5, 1, and 5 nM), and STLC (500 nM, 1 μM, and 5 μM); concentrations were selected for these drugs that produced a percentage of mitotic cells comparable to those observed with 50 to 500 nM PTX to generate samples for qXL-MS (Figure S1A).

Overview of Cross-Linking and Proteome-Level Quantitation

Real-time analysis for cross-linked peptide technology (ReACT) liquid chromatography-mass spectrometry (LC-MS) analysis (Weisbrod et al., 2013a) resulted in 3,900 non-redundant cross-links identified at an estimated false discovery rate (FDR) of 1% or less at the non-redundant cross-linked peptide pair level using probabilistic modeling with XLinkProphet (Keller et al., 2019a) (Table S1). The links represent 941 protein pairs, including intraprotein linkages. 3,134 (80%) of the cross-links were assigned as intraprotein, while 766 (20%) were interprotein links. On average, there were 6 cross-links detected per protein; 218 proteins had 5 or more cross-links, and 278 proteins had a single cross-link. All cross-link data and protein abundance-level data have been uploaded into XLinkDB and are accessible at the following URL: http://xlinkdb.gs.washington.edu/xlinkdb/HeLa_PTX_titration_Bruce.php (Keller et al., 2019b; Schweppe et al., 2016; Zheng et al., 2013). Within XLinkDB, an interactive network, quantitative values on the cross-link and protein levels, structural models, mass spectra, chromatograms, and more can be viewed. A total of 746 proteins were cross-linked and represent all major cellular compartments (Figure S1B). The distribution of cross-linked proteins across subcellular compartments matched previous XL-MS studies in HeLa cells (Chavez et al., 2013, 2015). Relative abundance levels for 683 of the 746 cross-linked proteins were obtained by global SILAC

analysis (Table S1). Data-dependent proteome analysis resulted in 3,195 identified proteins, with 2,935 quantified in at least one PTX concentration. 2,327 proteins were quantified in all seven drug concentrations applied (0, 5, 10, 20, 50, 100, and 500 nM PTX) (Table S2). Overall, the magnitude of protein-level changes observed due to PTX treatment was much less than that of the cross-link-level changes, indicating a larger effect on protein structures and interactions at relatively short time frames (18 h), in which minimal impact on protein abundance levels can occur. This also agrees with the observation that most changes to protein abundance levels occur in early G1 phase of the cell cycle, while most changes in protein stability, based on global proteome thermal profiling, occur in mitosis (Becher et al., 2018). In general, qXL-MS has higher variability than quantification of protein levels. Several factors contribute to this observation, including low abundance and signal-to-noise ratios of cross-links compared with non-cross-linked peptides and averaging of multiple quantified peptides per protein versus quantification of a single cross-linked peptide pair. Despite the inherent difficulties with XL-MS, clear changes to protein structures and interactions due to PTX treatment were visualized. To identify statistically meaningful cross-link changes responsive to PTX concentration, we applied multiple levels of statistical filtering. cross-links were filtered first to include those that were quantified in at least three of the drug concentrations with 95% confidence intervals of less than one (1,078), followed by longitudinal k-means clustering on the log2(PTX/DMSO) ratios. Clustering analysis resulting in three clusters was selected based on standardized criterion analysis (Figure 1; Figure S2). Figure S2 shows the mean trajectories for the three clusters representing cross-links that increase with PTX (22% of 1,078), those that are indifferent (49% of 1,078), and those that decrease with increasing PTX concentration (28.9% of 1,078). The reliability of this filtering is illustrated in volcano plots (Figure S3) showing the separation of the three clusters of cross-links. Due to the large size of this dataset, selected examples are discussed here. For data on specific proteins that are not covered here, we encourage readers to access the full dataset on XLinkDB. As with our previous study with Hsp90 inhibitors, we decided to initially look for expected changes by focusing on the primary drug target of PTX: tubulins.

Interaction of αβ-Tubulin

MTs, composed of αβ-tubulin heterodimers, are highly dynamic cytoskeletal filaments required for maintenance of cell morphology and cell division. MT dynamics are regulated by the binding and hydrolysis of guanosine triphosphate (GTP) to two sites within the αβ-tubulin heterodimer: the E-site (exchangeable) on β-tubulin at the + end of the MT and the N-site (non-exchangeable) on α-tubulin at the αβ-tubulin interface (Nogales et al., 1998). MT growth occurs preferentially at the + end as long as there is a sufficient concentration of GTP to maintain the GTP cap on the terminal β-tubulin subunits. Upon hydrolysis of GTP to guanosine diphosphate (GDP) at the E-site, rapid MT depolymerization ensues. PTX binds directly to β-tubulin, stabilizing the interaction with α-tubulin and preventing MT depolymerization (Alushin et al., 2014). Our results indicate that qXL-MS can detect the PTX-induced stabilization of MTs *in vivo*.

Multiple cross-links involving αβ-tubulin were detected and quantified with varying PTX concentration (Table S1). The data in Table S1 indicate missing ratios for many αβ-tubulin

cross-links, particularly at low PTX concentrations. This highlights the challenge with consistent quantification of the MS1 signal from very low abundance cross-links across multiple complex biological samples during an LC-MS analysis, in which MS2 and MS3 spectra are also acquired to identify the crosslinked peptide pair sequences. To fill in these missing values, we selected several αβ-tubulin cross-linked peptide pairs for targeted analysis with parallel reaction monitoring (PRM), which has higher sensitivity, allowing consistent quantification across samples as previously demonstrated for Hsp90 (Chavez et al., 2016a). PRM uses accurate mass and time information for the αβ-tubulin cross-links as probes for MT dynamics. Mapping the observed αβ-tubulin cross-links onto the cryoelectron microscopy (cryo-EM) structure of MTs stabilized by PTX (PDB: 3J6C) (Alushin et al., 2014) illustrates that the link between α-tubulin K326 and β-tubulin K216 lies near the αβ-interaction interface, E-site, and PTX binding site with a measured Euclidean Cα-Cβ distance of 15.1 Å (Figure 2A). The cross-link between α-tubulin K370 and β-tubulin K58 spans a longer distance: 52.3 Å when mapped to the same αβ-tubulin pair as the K216-K326 link or 35.8 Å when mapped to another αβ-tubulin subunit within the MT assembly (Figure 2A). Because the 52.3 Å distance is longer than the maximal cross-linkable distance between residues for the cross-linker used in this study, biotin aspartate proline-N-hydroxyphthalamide (BDP-NHP) maximal distance = 42.1 Å (Chavez et al., 2018), the K370-K58 link is likely formed across a lateral contact between αβ-tubulin dimers reflective of the higher-order assembly, in agreement with the MT structural model in the PDB (PDB: 3J6C). It has been suggested that the seams along the lateral contacts may represent a weak spot in the MT structure, in which initiation of depolymerization can occur upon GTP hydrolysis (Alushin et al., 2014). Two distinct peptide sequences from α-tubulin, differing by the second amino acid residue (ISVYYNEATGG**K58**YVPR from TBB5 and INVYYNEATGG**K58**YVPR from TBB4B), identify the K370-K58 αβ-tubulin linkage (Figure S4; Table S1), indicating that differing β-tubulin isoforms occupy a conformation similar to that of α-tubulin with the assembled MT. These cross-links identifying both β-tubulin isoforms display a similar increasing dose-dependent response with PTX treatment (Figures 2B and 2C). In addition, two distinct cross-links between K60 and K370 in α-tubulin differ in sequence for the K60-containing peptide by two amino acids (TIGGGDDSFNTFFSETGAG**K60**HVPR and TIGGGDDSFTTFFCETGAG**K60**HVPR), uniquely identifying this link in different isoforms of α-tubulin, TBA1A and TBA4A, respectively. While the K60-K370 links are assigned as α-tubulin intraprotein linkages and the intralink distance is consistent with the structure shown in Figure 2A (Cα-Cα distance of 29.0 Å), they are also consistent with links between lateral contacting α-tubulin subunits (Cα-Cα distance of 16.6 Å) within the assembled MT. The observed large increase in the K60-K370 links with increasing PTX concentration, much greater than the TBA1A and TBA4A protein levels, is in agreement with PTX-induced MT stabilization (Figure 2B). Importantly, several cross-links, including the K60-K370 link, displayed no change in levels when the cells were treated with the KIF11 inhibitor STLC or the MT destabilizer CA4, supporting the conclusion that the observed increase is specific to PTX stabilization of MTs (Figure 2C; Table S1). No tubulin cross-links were detected in the NOC-treated sample. The specific tubulin isoform composition of MT has been shown to tune MT dynamics (Vemu et al., 2017) and contribute to PTX resistance in cancer (Albrethsen et al., 2014; Kavallaris et al., 1997). The observed increases in the cross-link levels reflect increased interaction

between α-tubulin and β-tubulin despite relatively minor increases in protein levels for the various tubulin isoforms with PTX treatment (Figures 2B and 2C). These results support the expected outcome of PTX stabilization of MTs, providing a level of confidence to explore PTX-induced changes evident in the dataset.

Effects on Cytoskeletal Proteins

In addition to MT, the other two major classes of cytoskeletal filaments are actin microfilaments (MFs) and keratin intermediate filaments (IFs). MFs are essential for cell motility, cytokinesis, and many other processes vital for cancer progression. IF proteins are often overexpressed in cancer cells and can contribute to multidrug-resistant phenotypes (Bauman et al., 1994). While these other two classes of cytoskeletal filaments are viable targets for chemotherapy, all currently approved drugs targeting cytoskeletal proteins used in the clinical setting are primarily directed at MTs (Trendowski, 2014). PTX is known to also have effects on MFs and IFs, although the molecular details of these changes are not as well characterized as with MTs (Herman et al., 1983). With qXL-MS, we observed structural and interaction changes among both of these cytoskeletal filament components in response to PTX treatment.

Multiple cross-links involving actin (ACTB) were measured with increasing levels with PTX treatment. In particular, five cross-links involving K328 of ACTB, including an unambiguous homodimer linkage, and links between K328-K61 and K328-K315 all increased with PTX concentration (Figure 3A). As observed with the tubulins, the increases for the cross-links were much larger than any change in protein level, indicating conformational/interaction changes in ACTB (Figure 3A). In a previous study applying XL-MS in mouse heart tissue, K328 was observed to be a relative hotspot of cross-linking in mouse homolog ACTA and involved in links indicating conformational plasticity of sarcomere complexes (Chavez et al., 2018). Comparing these links to structural models for actin filaments in the PDB, only the K328-K315 link is compatible with an intramolecular link within a single ACTB monomer (Figure 3B). The spatial arrangement and distance between K328 and K61 is consistent with a link between neighboring ACTB subunits within the MF structure. The homodimeric K328 link is not compatible with any measured Cα-Cα distance between K328 residues on neighboring ACTB subunits within any actin MF structure evaluated from the PDB (Figure 3B). Cross-links that exceed the expected distance constraints have been shown to represent different conformations of proteins and protein complexes within the greater existent ensemble of structures (Ding et al., 2017). So-called overlength cross-links have proven useful for evaluation of induced conformational shifts in three purified enzymes (calmodulin, enzyme I, and glutamine binding protein) (Ding et al., 2017), shifting Hsp90 conformations induced by inhibitor treatment (Chavez et al., 2016b), as well as differing troponin-actin interactions from heart tissue (Chavez et al., 2018). This K328 homodimeric link could potentially form between actin subunits existing in separate MFs, where they cross as part of the cytoskeletal structure or as MF bundles. Interestingly, formation of circular rings of actin bundles has been observed by microscopy upon PTX treatment of fibroblast and MCF7 breast cancer cells (Pletjushkina et al., 1994; Rosenblum and Shivers, 2000). The observed changes involving actin are PTX or drug specific, unlike

those resulting from general mitotic arrest, because treatment with NOC, CA4, and STLC did not produce the same observed changes (Figure 3C).

IFs are composed of cytokeratins, which form obligate heterodimer complexes between type 1 (acidic, keratins 9–28) and type 2 (basic, keratins 1–8 and 71–80), often displaying interdependent stability and expression (Karantza, 2011). The structural framework of IFs protects cells from both mechanical and cytotoxic stress, including treatment with chemotherapy drugs. Keratins assemble in parallel as type 1/2 heterodimers. These parallel dimers can further oligomerize as tetramers in an anti-parallel manner. Previously, increased levels and interactions keratin 8/18 were found to be associated with a multidrug-resistant phenotype (Chavez et al., 2015). In cells undergoing apoptosis, the keratin 8/18 IF network is rapidly reorganized by caspase-directed cleavage of keratin 18, resulting in the formation of keratin fragments that aggregate and are excreted from cells in the latter stages of apoptosis (Caulín et al., 1997). Each of the three keratins (K1C18, K2C7, and K2C8) displayed similar trends in protein abundance level, generally increasing to a maximum log2(PTX/DMSO) of between 0.4 and 0.8 at 100 nM PTX (Figure 4A). The quantified cross-links involving keratins displayed changes independent of the observed changes in the protein abundances. The K1C18, K2C8, and K2C7 cross-links are displayed as an interaction network, in which the links are colored according to the k-means cluster representing the general trend they followed with increasing PTX concentration, that is, generally increasing (yellow), no change (black), or decreasing (blue) (Figure 4B). A total of 27 cross-linked peptide pairs involving K2C7, K2C8, and K1C18 increased with increasing PTX treatment (Figure 4B). These included 3 links between K1C18 and K2C7, 10 links between K1C18 and K2C8, 3 links within K1C18, and 11 links within K2C8.26 links displayed no change in relative levels across the PTX concentrations tested, while 28 links decreased with increasing PTX. Three unambiguous homodimeric cross-linked peptide pairs, two involving K111 of K1C18 (LES$\mathbf{K^{111}}$IR and the missed tryptic cleavage form RLES$\mathbf{K^{111}}$IR) and one involving K130 of K2C8, displayed decreasing trends with PTX; however, another homodimeric link at K325 of K2C8 showed no change. PTX has been shown to induce formation of aggregates of intertwining IFs, which displayed a complementary cellular distribution to bundles of MTs (Forry-Schaudies et al., 1986). These changes in cross-links involving IFs appear largely specific for PTX, because treatment with NOC, CA4, and STLC produced different quantitative patterns, as seen in the heatmap in Figure 4C.

We detected a cross-link between K7307 of microtubule-actin cross-linking factor 1 (MACF1) and K1932 of protein AHNAK2 (AHNK2) that displayed a dose-dependent decrease with increasing PTX, despite no change to either of the protein levels (Figure S5). Both proteins are large multidomain scaffolding proteins not previously reported to interact with each other. MACF1 is a (~800 kDa) plakin protein that bridges MTs and MFs dynamically (Goryunov and Liem, 2016). AHNK2 is a (~600 kDa) multidomain scaffolding protein functioning in membrane repair and calcium signaling (Komuro et al., 2004). MACF1, K7307 resides near the C terminus in a MT binding domain (Figure S5B). AHNK2, K1932 occurs in 1 of 24 repeat motifs proposed to form β-propeller domains (Figure S5) (Komuro et al., 2004). MACF1 and AHNK2 were also cross-linked to histone

H3. K2209 of MACF1 was also cross-linked to two sites in the middle domain of HS90B. Although not a direct target of PTX, MACF1 has been shown to be indirectly affected and differentially responsive to MT-targeting drugs (Quick, 2018). MACF1 is associated with several diseases, including cancer, suggesting it could be a useful therapeutic target for future drug development (Afghani et al., 2017; Miao et al., 2017; Quick, 2018). AHNK2 is an oncogenic protein and prognostic marker in several carcinomas, including pancreatic ductal adenocarcinoma (PDAC), a highly aggressive and malignant disease that is currently the fourth-leading cause of cancer deaths worldwide (Bhasin et al., 2016; Garrido-Laguna and Hidalgo, 2015; Klett et al., 2018; Lu etal., 2017; Wang etal., 2017). Taxanes, including PTX, have been shown to exhibit beneficial, synergistic effects when used in combination with gemcitabine and other drugs for the treatment of PDAC, although effective drug delivery and management of toxicity of these drugs still presents significant issues in their use (Adamska et al., 2017). The sensitivity of MACF1 and AHNK2 interactions to PTX may provide useful information in the continued quest for advanced therapeutics.

Receptor-Type Tyrosine-Protein Phosphatase F

The receptor-type tyrosine-protein phosphatase F (PTPRF, aka LAR), is a plasma membrane-bound protein involved in cell adhesion and cellular signaling (Xu and Fisher, 2012). PTPRF localizes to and regulates the assembly of focal adhesions, large multiprotein complexes that link the actin cytoskeleton to the extracellular matrix (Sarhan et al., 2016). PTPRF contains an N-terminal extracellular region consisting of three immunoglobulin (Ig)-like domains and eight repeating fibronectin type III (FnIII) domains (Figure S6A). A transmembrane region connects the extracellular region to the intracellular C-terminal region consisting of two phosphatase domains: the catalytically active (D1) and the catalytically inactive (D2) (Um and Ko, 2013). The expression level of PTPRF has been suggested as a potential prognostic marker in non-small-cell lung cancer treatments involving the receptor tyrosine kinase inhibitor erotinib (Soulières et al., 2015). Four cross-links from PTPRF were identified and mapped to approximate locations within the domain architecture of PTPRF (Figure S6A). Three cross-links in PTPRF decreased with increasing PTX, including the links between K906-K994 and K979-K1016 (Figure S6B). A third link, K895-K872, displayed a similar decrease, although no confidence intervals were obtained for the quantitation of this link. These three cross-links originate in the extracellular, FnIII repeat region of PTPRF (K895-K872 in FnIII 6, K906-K994 spanning FnIII 6 and FnIII 7, and K979-K1016 spanning FnIII 7 and FnIII 8). These three cross-links decrease despite no change in PTPRF abundance (Figure S6B). PTX treatment appears to decrease the link between K906 and K994 to a greater extent than observed with NOC, CA4, or STLC, suggesting drug-specific conformational changes in the PTPRF FnIII domain (Figure S6C). In contrast, a cross-link in the intracellular, D1 phosphatase domain (K1455-K1459) displays increasing levels with PTX. PTPRF is a crucial component of mitotic retraction fibers, actin-rich remnants of focal adhesions that maintain attachment between the mitotic cells and the extracellular matrix and position the mitotic spindle according to extracellular stimuli (St-Denis et al., 2016). Importantly, small interfering RNA (siRNA) depletion of PTPRF results in formation of multipolar spindles and chromosome misalignment, as observed in PTX-induced cell death (St-Denis et al., 2016; Zasadil et al., 2014). The PTX-

induced conformational changes within multiple PTPRF domains may contribute to PTX cytotoxicity.

Altogether, the quantitative results on cross-link and protein levels for the selected examples of cytoskeletal proteins discussed earlier demonstrate that PTX treatment has widespread effects on the conformation and interactions of these proteins beyond the primary target of MTs. Furthermore, the observed changes in the cross-links are greater than, and in some cases display differing trends to, the changes in protein abundance levels.

Mitochondrial Proteins

Mitochondria function primarily as the cells' power plant, producing the bulk of cellular chemical energy in the form of ATP. Instead of relying on mitochondrial-generated ATP, cancer cells use glycolysis for most of their ATP through what is known as the Warburg effect (Liberti and Locasale, 2016). Mitochondria are also key regulators of apoptosis and influence the cells' response to chemotherapy drugs (Lopez and Tait, 2015; Sarosiek et al., 2013). PTX increases the mitochondrial membrane potential (ψ) by decreasing free cytosolic tubulin, which leads to opening of the voltage-dependent anion channels (VDACs) on the outer mitochondrial membrane (Maldonado et al., 2010). Cross-links spanning the β-barrel pores of VDAC1 and VDAC2 increased with higher PTX concentration, potentially reflective of drug-induced conformational changes related to channel opening (Figures S7A–S7E). The increased VDAC links appear specific to PTX, because treatment with NOC, CA4, and STLC did not produce the same effect (Figure S7E). To assess the effect of PTX on mitochondrial function and bioenergetics, we measured the oxygen consumption rate (OCR) of HeLa cells treated with varying concentrations of PTX (0, 5, 10, 20, and 500 nM) (Figure S7F). We observed decreased basal, ATP synthase-driven, and maximal respiration rates compared with a vehicle control at all PTX concentrations tested. Interestingly, the maximal OCR at the highest PTX concentration tested was equivalent to the control despite reduced basal and ATP synthase-driven OCR. Increased respiratory reserve capacity (maximal-basal OCR), is a mechanism for cells to cope with increased stress due to drug treatment and resist cell death (Pfleger et al., 2015; Teh et al., 2019). Increased reserve capacity has been observed with development of acquired resistance to PTX by long-term exposure to low concentrations (10 nM) (Datta et al., 2017). Clearly, PTX induced changes to mitochondrial function, as revealed by OCR measurements, and qXL-MS can help elucidate PTX-mediated mitochondrial interactome changes.

ATP Synthase

ATP synthase (oxidative phosphorylation [OXPHOS] complex V [CV]) primarily functions to generate ATP from ADP by oxidative phosphorylation, using the proton motive force from the electron transport chain and ψ to drive its function. In addition, CV is important in maintaining the cristae structure of the inner mitochondrial membrane and plays a critical role in the formation of the mitochondrial permeability transition pore (mPTP). OCR measurements indicated PTX lowered ATP-driven mitochondrial respiration. This is interesting in light of a report that the PTX-induced increase in ψ is maintained by ATP hydrolysis by CV working in reverse (Maldonado et al., 2016). Five cross-links within CV increased with PTX treatment (Figure 5A). Currently, there is no available structure in the

PDB for human CV, so the human sequences were aligned against the bovine CV sequence structure (PDB: 5ARA) (Figure 5B). Two of the increasing links are between the CV α subunit (ATPA) and the CV β subunit (ATPB), which assemble as a heterohexamer constituting the core of the F_1 portion of CV. The catalytic site of CV in which ADP is phosphorylated to ATP exists at the interface between ATPA and ATPB. Two additional cross-links, including one with an additional missed tryptic cleavage site, identify a link between ATPB K124 and CV O subunit (ATPO, aka the oligomycin sensitivity conferring protein [OSCP]) K192. The strong increase in the cross-link levels, log2(PTX/DMSO) of between 1 and 2.5, is larger than the modest increase in protein levels observed for ATPA, ATPB, and ATPO (log2[PTX/DMSO] of ~0.5), suggesting conformational/interaction-level changes within CV beyond protein expression (Figure 5A). These observed changes reflect structural changes in CV as a result of the PTX effects on mitochondrial bioenergetics and correlate with decreased CV-driven respiration (Figure 5C). Hyperpolarization of mitochondria and resulting high levels of ATP are important for the maintenance of the apoptotic microtubule network (AMN), a critical cytoskeletal structure that preserves cell morphology and plasma membrane integrity in cells undergoing apoptosis (Oropesa et al., 2011). Furthermore, PTX stabilizes the AMN and prevents the depolarization of ψ (Oropesa et al., 2011). At relatively high concentrations (1–20 μM), PTX induces production of reactive oxygen species (ROS) and mPTP opening, followed by collapse of ψ and ultimate cell death (Varbiro et al., 2001).

Prohibitins

The PHBs are an obligate, ubiquitously expressed pair of proteins: prohibitin 1 (PHB) and prohibitin 2 (PHB2). PHBs are multifunctional proteins with many attributed roles, including proliferation, regulation of transcription, apoptosis, chaperoning, and cellular senescence in various intracellular locations, including the nucleus, mitochondria, and cytosol (Bavelloni et al., 2015). However, the relationship between the cellular localization of PHBs and the many attributed functions remains a mystery. Currently, there are no high-resolution structural models available for PHBs, which have been noted to be difficult to crystalize (Winter et al., 2007). PHBs are thought to contain 3 domains: a N-terminal transmembrane domain, a PHB domain, and a coiled-coil domain (Winter et al., 2007). Electron microscopy experiments show that in the mitochondrial inner membrane, PHBs assemble into large 1.2 MDa ring structures consisting of 16–20 PHB-PHB2 dimers (Tatsuta et al., 2005).

PHB plays a role in tyrosine kinase signaling pathways, and defects in PHB tyrosine phosphorylation can lead to the development of diseases, including cancer and diabetes (Ande et al., 2017). Subcellular shuttling of PHBs play a critical role in cell survival and apoptosis (Peng et al., 2015). PHB has been shown to act as a mediator of PTX resistance by changing subcellular localization (Patel et al., 2010). In PTX-resistant lung cancer cells, PHB was found to be localized primarily in the mitochondria and plasma membrane, and siRNA knockdown of PHB resulted in activation of apoptosis in response to PTX treatment (Patel et al., 2010). Rocaglamides, potent anticancer drugs in the flavagline family, bind directly to PHBs localized to the plasma membrane, preventing interaction with the protein kinase CRaf and thereby inhibiting downstream activation of the Raf-MEK-ERK signaling

pathway, mediating cell-cycle progression and proliferation in cancer cells (Polier et al., 2012).

A total of 16 non-redundant cross-links were identified involving PHB and PHB2. These included 8 interprotein cross-links between PHB and PHB2 corresponding to 6 Lys-Lys pairs occurring in both the PHB domains and the coiled-coil domains. Two cross-links identified unambiguous homodimeric links at K202 of PHB. Homodimeric links in PHB2 were identified at K250 and K262. k-means clustering revealed that 5 of the 8 interprotein links increased levels with increasing PTX, while intraprotein links between K216-K262 and K244-K296 in PHB2 did not change (Figure 6A). Two unambiguous homodimeric links at K202 of PHB increased with PTX. A similar increase in the K202 PHB homodimeric link was observed with STLC treatment. One link contains two fully tryptic sequences (FVVE**K^{202}**AEQQK), while the second homodimeric link contains a missed tryptic cleavage site on one peptide (FVVE**K^{202}**AEQQKK) of the cross-linked pair. Cross-links containing both forms of the PHB K202 peptides were involved in interprotein linkages with K216 and K262 of PHB2 and displayed similar increasing trends with increasing PTX concentration (Figures 6A and 6B). In contrast, both PHB2 K216 to PHB K202 links remained unchanged when cells were treated with either CA4 or STLC. Similarly, the fully tryptic PHB K202 to PHB2 K262 cross-linked peptide pair was unchanged with CA4 or STLC treatment; however, the form with a missed cleavage on the K202-containing peptide was observed to increase with these other inhibitors (Figure 6C). Both PHB and PHB2 displayed relatively minor increases (log2[PTX/DMSO] of ~0.5) in protein levels at PTX concentrations above 50 nM (Figure 6B). Altogether, changes in cross-link levels were greater than the PHB or PHB2 protein level increases (Figure 6B). This could be indicative of increased PHB-PHB2 complex levels and/or reflective of changes to subcellular localization.

Chaperones and Heat Shock Proteins

Hsp90 is an important molecular chaperone that helps to ensure integrity of the proteome, functioning to maintain and properly fold hundreds of client proteins (Trepel et al., 2010). Cancer cells are heavily reliant on Hsp90, because it stabilizes numerous oncoproteins. Therefore, effort has been devoted to the development of Hsp90 inhibitors for cancer treatment (Neckers and Workman, 2012). The primary two isoforms of Hsp90 are the inducible form, Hsp90-α (HS90A), and the constitutively expressed Hsp90-β (HS90B). These two isoforms have specific sets of client proteins and display differing effects to inhibitors. *In vivo*, Hsp90 is primarily assembled as a dimer, the homodimeric α-α and β-β or the mixed dimer α-β. The dimer functions in concert with several co-chaperones, including Hsp70, Hsp40, STIP, and Aha1. One issue with the clinical application of classical Hsp90 inhibitors, which bind to the ATP pocket in the Hsp90 N-terminal domain, is the resulting activation of heat shock response (HSR). HSR induces high expression levels of HS90A, Hsp70, Hsp40, and Hsp27, protecting cancer cells from apoptosis. Drugs that target the Hsp90 C-terminal domain, including novobiocin, have been shown to avoid the HSR (Bhatia et al., 2018; Donnelly and Blagg, 2008; Eskew et al., 2011). PTX also binds to Hsp90 in the C-terminal domain, where in contrast with traditional Hsp90 inhibitors, PTX has a stimulating effect on Hsp90 (Donnelly and Blagg, 2008). Indeed, we see no indication

of HSR activation by PTX treatment, as evidenced by Hsp90 and Hsp70 protein levels (Figure 7B). Of the 42 non-redundant cross-links involving Hsp90 that were repeatedly quantified, most (30) displayed no significant change, while 8 decreased and 4 increased with PTX (Figure 7A). Among the decreasing links is a HS90A homodimeric link at K443. However, the homologous homodimeric link on HS90B at K435 was unchanged by PTX. HS90A-HS90B heterodimeric links involving HS90A K443 to HS90B K435 and HS90A K443 to HS90B K347 also displayed decreasing trends with increasing PTX concentration. These differential effects on dimerization are interesting considering that HS90A and HS90B have different dimerization potentials (Csermely et al., 1998). Two peptide pairs identifying a HS90B homodimeric link at K607 decreased with increasing PTX concentration. K607 of HS90B exists in a flexible region, between the middle and the C-terminal domains, which is important for interactions with client proteins (Verba et al., 2016).

Independent of PTX binding to β-tubulin, PTX was shown to bind to Hsp90 and activate macrophages in a manner indistinguishable from bacterial lipopolysaccharide (Byrd et al., 1999). This observed macrophage-activating effect was blocked by the Hsp90 inhibitor geldanamycin (Byrd et al., 1999). The geldanamycin derivative 17-allylamino-17-demethoxygeldanamycin (17-AAG) was demonstrated to act synergistically with PTX, sensitizing cancer cells to PTX (Solit et al., 2003). We previously investigated the effect of 17-AAG on Hsp90 in cells using the same qXL-MS approach used in the current study (Chavez et al., 2016b). By comparing the results from the previous 17-AAG study with the PTX-, NOC-, CA4-, and STLC-induced changes to Hsp90 cross-links in the current results, we can gain insight into the distinct drug-induced structural changes in Hsp90. Quantifying cross-links revealed unique effects on Hsp90 with the five drugs, as shown in Figure 7C. Key differences observed between 17-AAG and PTX include the HS90A homodimeric link at K443, which was greatly increased with 17-AAG yet decreased with PTX and remained unchanged with STLC. Similarly, the heterodimeric link between HS90A K443 and HS90B K435 increased with 17-AAG, decreased with PTX, and remained unchanged with NOC, CA4, and STLC. In contrast, the HS90B K435 homodimeric link was unchanged by any drug (Figure 7C). Links that increase with 17-AAG yet remain unchanged by PTX include the link between HS90B K354-K284 and HS90A K615-K443 (Figure 7C). Overall these results highlight differential conformational and interaction effects induced on Hsp90 by 17-AAG and mitotic inhibitors. Cancer cells are generally more sensitive to Hsp90 inhibitors than normal cells. Recent evidence suggests this difference is related to cell-cycle activity, with quiescent cells being less sensitive than actively proliferating cells (Echeverria et al., 2019). Therefore, cells locked in mitosis by PTX or other inhibitors could be in a primed state, making them more susceptible to apoptosis induced by Hsp90 inhibitors. Regardless of the mechanism, the results presented here demonstrate that qXL-MS can detect distinct drug-induced changes to the conformation of Hsp90 independent of changes in protein abundance.

DISCUSSION

The combination of SILAC with qXL-MS allows large-scale measurements to be made on relative protein abundances, protein conformations, and interactions that change within cells

when they are perturbed with drugs. Importantly, this allows visualization of changes to protein conformations and interactions that occur independent of changes in protein abundance. In this study, we used this technique to investigate the effects of PTX treatment in cells. To distinguish PTX-specific changes from those due to general mitotic arrest, we employed different mitotic inhibitors: NOC, CA4, and STLC. We found that most cross-links identified and quantified in this study displayed no response to PTX treatment. Smaller fractions displayed either decreasing (29%) or increasing (22%) trends in their relative abundances with increasing PTX concentration. Overall, the changes observed in the levels of cross-linked peptide pairs were more drastic than the changes in protein abundance. Furthermore, we observed multiple examples in which changes in cross-link levels displayed PTX-dependent changes while the protein abundance was unchanged, indicative of drug-induced conformational and interaction changes.

In agreement with the primary mode of action for PTX, we observed a PTX dose-dependent response of cross-links in α and β-tubulins, reflective of drug-induced stabilization of MTs, a feature that was not observed with other mitotic inhibitors. The results also demonstrate that cross-linked peptide pairs can in some cases distinguish between tubulin isoforms, an important aspect that could be useful for future studies investigating MT dynamics. Beyond PTX rearrangements of MTs, other cytoskeletal components, including MFs, IFs, and the cell surface receptor protein PTPRF, displayed PTX-specific changes. In addition, we demonstrate that PTX alters mitochondrial respiration with quantified cross-links, indicating conformational changes to mitochondrial proteins/protein complexes, including CV, PHBs, and VDAC. With the importance of each of these proteins in cancer and apoptotic signaling, the PTX concentration-dependent changes revealed through the quantified cross-linked peptide pairs provide evidence of the widespread cellular response to PTX.

In summary, the results in this report reveal PTX-induced interactome dynamics in cells and are in agreement with, and expand upon, results of multiple previous studies indicating that PTX exerts some effects on these various proteins by providing quantitative structural information to accompany the changes. Mitotic inhibitor-induced changes to Hsp90 were observed and compared with previous results using 17-AAG, highlighting the ability to visualize drug-specific changes. These observations indicate that drug-induced interactome dynamics provide drug target- and drug mechanism-specific large-scale information on protein conformations and interactions to improve understanding of pharmacological effects. Continued improvements in this approach, including molecular design, sample preparation, and mass spectrometry methods, will yield increasingly greater detail on relevant interactome dynamics.

STAR★METHODS

LEAD CONTACT AND MATERIALS AVAILABILITY

This study did not generate new unique reagents. Further information and requests for resources and reagents should be directed to and will be fulfilled by the Lead Contact, James E. Bruce (jimbruce@uw.edu)

EXPERIMENTAL MODEL AND SUBJECT DETAILS

HeLa cell line—HeLa cells (ATCC) were seeded at a density of 5×10^6 cells into 150 mm culture dishes with 20 mL of SILAC DMEM medium containing either isotopically light L-lysine and L-arginine or isotopically heavy $^{13}C_6{}^{15}N_2$-L-lysine and $^{13}C_6$-L-arginine (Silantes) and supplemented with 10% dialyzed FBS (Valley Biomedical Inc.) and 1% penicillin/streptomycin (Fisher Scientific).

METHOD DETAILS

Mitotic inhibitor treatment—HeLa cells, cultured as described above, were treated with various concentrations (5, 10, 20, 50, 100, 500 nM) paclitaxel (PTX, Fisher), 3 μm nocodazole (NOC), 5 μm S-trityl-L-cysteine (STLC), 5 nM combretastatin A-4 (CA4), or 0.1% v/v dimethyl sulfoxide (DMSO) for 18 h before harvesting from the plates with 5 mL of phosphate buffered saline (PBS) (Fisher Scientific) containing 5 mM EDTA. Cells were washed with PBS and pelleted by centrifugation at 300 g for 3 min. Cell pellets were then suspended in 170 mM Na_2HPO_4 pH 8.0 in preparation for chemical cross-linking.

Live cell imaging—Cells were cultured under conditions as described in the preceding section in 96 well plates. Live cell imaging was performed using a Cytation 5 imaging system (Biotek) using a 4x objective. High contrast brightfield imaging for label free live cell proliferation measurements was accomplished by capturing two high contrast brightfield images at each time point, one in focus image for reference and a defocused image, with an offset of −250 μm from the in focal plane, for cell counting. Images were processed with Gen 5 to get total cell counts as well as counts of mitotic cells which have a relatively high circularity compared with cells in other cell cycle phases. For cellular analysis the defocused brightfield image was processed using a dark background setting and a flattening size of 10 μm. A primary mask was applied using a threshold of 5,000 relative intensity units along with background percentage of 5%, a minimum object size of 5 μm and a maximum object size of 50 μm. Identification of mitotic cells was accomplished by applying a secondary mask to the images, selecting for objects with a circularity of 0.5 or greater with an area of less than 500 as well as an intensity of 18000 or more.

Synthesis of cross-linker—The PIR cross-linker Biotin Aspartate Proline - N-hydroxyphthalamide (BDP-NHP) (Chavez et al., 2019) was synthesized by solid phase peptide synthesis using a Liberty Lite peptide synthesizer (CEM). FMOC N-terminal protected amino acids were coupled in the following order biotin Lys, Lys, Pro, Asp, succinic anhydride on Gly-SASRIN resin. Dimethyl formamide (DMF) was used as the solvent for all solutions. The coupling reagents consisted of 0.5 M diisopropylcarboimide and 1 M ethyl 2-cyano-2-(hydroxyi-mino)acetate (Oxyma). A solution of 20% (v/v) piperidine was used as the deprotection reagent. After the succinate coupling step the resin containing the peptide was transferred to a 50 mL conical tube and swelled with a minimal volume of DMF. A 12-fold molar excess of the trifluoroacetate ester of N-hydroxyphthalamide (TFA-NHP) was dissolved in 10 mL of dry pyridine and added to the resin. The mixture was allowed to react for 20 min at room temperature with constant mixing at 700 rpm using a Thermomixer R (Eppendorf). The mixture was then transferred to a Poly-Prep chromatography column (Bio-Rad) and the solution was removed by vacuum

filtration. The resin was washed with 30 mL of DMF followed by 30 mL of dichoromethane (DCM). The cross-linker was then cleaved from the resin using 2 mL of a 95% TFA 5% DCM solution and incubating for 3 h at room temperature with constant rotation. The solution was then collected into a clean 2 mL Eppendorf tube. The cross-linker was precipitated by adding the solution containing the cross-linker to 40 mL of diethyl ether cooled to −80°C. The cross-linker was pelleted by centrifugation for 20 min at 3000 g. The diethyl ether was removed and the pellet was resuspended in a fresh 40 mL aliquot of cold ether. The ether was repeated once more then the cross-linker pellet was dried by vacuum centrifugation using an EZ2-Plus evaporator (Genevac). The purified cross-linker was then dissolved in DMSO to a concentration of 268 mM and stored at −80°C until used.

Chemical cross-linking of SILAC cells—Isotopically light and heavy cells were mixed at equal numbers (2×10^7 cells) in biological replicates, either light PTX treated/ heavy control (treated with 0.1% by volume of DMSO) or light control/ heavy PTX treated, before adding the PIR cross-linker (Biotin Aspartate Proline - N-hydroxyphthalamide, BDP-NHP), synthesized by solid phase peptide synthesis as described above, from a concentrated stock solution (268 mM) in DMSO to a final concentration of 10 mM. The reaction was carried out at room temperature for 1 h with constant mixing. After 1 h the cells were pelleted by centrifugation at 300 g for 3 min the supernatant was removed and the cells were washed to remove hydrolyzed cross-linker by suspending the cell pellet in 1 mL 0.1 M NH_4HCO_3 pH 8.0. The cells were repeatedly pelleted and washed with fresh 0.1 M NH_4HCO_3 buffer until no yellow color (due to NHP) remained in the supernatant (total of 3–4 pellet/resuspension cycles per sample). After the final wash, cells were pelleted the supernatant was removed and the cell pellet was stored at −80°C until further processing.

Cell lysis and cross-linked peptide sample preparation—Cells were lysed by resuspending the cross-linked cell pellet in 0.5 mL of 8M urea, 0.1M NH_4HCO_3. Sample viscosity was reduced by sonication using a GE-130 ultrasonic processor to apply five sequential 5 s pulses with an amplitude between 40 and 80. Reduction and alkylation of cysteine residues was accomplished by incubation with 5 mM tris(2-carboxyethyl)phosphine (TCEP) (Fisher Scientific) for 30 minutes followed by a 45 minute incubation with 10 mM iodoacetamide (Fisher Scientific). To reduce the urea concentration to less than 1 M the samples were diluted by a factor of 10 with fresh 0.1 M NH_4HCO_3 buffer pH 8.0. The protein concentration was measured using the Pierce Coomassie protein assay (Thermo). Samples containing 5 mg of total protein were enzymatically digested by adding a 1:200 ratio of sequencing grade modified trypsin (Promega) to protein and incubating at 37°C for 18 hr. Peptide samples were acidified to pH 2 with trifluoroacetic acid before desalting by solid phase extraction using C18 Sep-Pak cartridges (Waters). Desalted samples were concentrated by vacuum centrifugation using an EZ2-Plus evaporator. Peptide samples were then adjusted to a volume of 0.5 mL with 7 mM KH_2PO_4, 30% acetonitrile pH 2.8 before being fractionated by strong cation exchange chromatography (SCX) using an Agilent 1200 series HPLC system equipped with a 250×10.0 μm column packed with Luna 5 μm 100A particles (Phenomenex). Peptide separation was accomplished using a binary mobile phase solvent system consisting of solvent A (7 mM KH_2PO_4, 30% acetonitrile pH 2.8) and solvent B (7 mM KH_2PO_4, 350 mM KCl, 30% acetonitrile pH 2.8) at a flow rate of 1.5

mL/min using the following gradient program: 0–7.5 min 100% A, 7.5–47.5 min 95% A/5% B to 40% A/ 60% B, 47.5–67.5 min 40% A/ 60% B to 100% B, 67.5–77.5 min 100% B, 77.5–97.5 min 100% A. A total of 15 fractions (5 min time slices, 7.5 mL each) were collected starting after an initial 17.5 min delay. Resulting SCX fractions were concentrated by vacuum centrifugation before their pH was adjusted to 8.0 by the addition of 0.1 M NH$_4$HCO$_3$. Fractions 6 and 7 were combined as well as fractions 11–14. To each of five fractions (6–7, 8, 9, 10, 11–14) 200 μL of monomeric avidin slurry (Thermo) was added and the samples were mixed for 30 minutes at room temperature. To remove non-biotin containing peptides the avidin beads were washed 3 × with 3 mL 100 mM NH$_4$HCO$_3$ pH 8.0 before eluting the cross-linked peptides by incubating the beads for five minutes each with two 500 uL aliquots of 70% acetonitrile, 30% H20 containing 0.5% formic acid. The enriched cross-linked peptide sample was then concentrated by vacuum centrifugation and stored at −80°C until LC-MS analysis. Samples containing non-cross-linked peptides present in SCX fractions 1–5 were used for relative protein abundance level analysis as described in the relevant section below.

LC-MS^n analysis of cross-linked peptide pairs—Samples containing PIR cross-linked peptides were analyzed in technical triplicate by liquid chromatography mass spectrometry using a NanoAcquity UPLC (Waters) coupled to a Velos-FTICR mass spectrometer (Thermo Scientific) (Weisbrod et al., 2013b) and a real-time adaptive, targeted mass spectrometry method developed for PIR cross-linked peptides(Weisbrod et al., 2013a). Peptides were loaded onto a 3 cm × 100 μm inner diameter fused silica trap column packed with a stationary phase consisting of with 5 μm Reprosil C8 particles with 120 Å pores (Dr. Maisch GmbH) with a flow rate of 2 μL/ min-1 of mobile phase consisting of 98% solvent A (H2O containing 0.1% formic acid) and 2% solvent B (ACN containing 0.1% formic acid) for 10 minutes. Peptides were then fractionated over a 60 cm × 75 μm inner diameter fused silica analytical column packed with 5 μm Reprosil C8 particles with 120 Å pores by applying a linear gradient from 95% solvent A, 5% solvent B to 60% solvent A, 40% solvent B over either 120 or 240 minutes at a flow rate of 300 nL/min. Eluting peptide ions were ionized by electrospray ionization by applying a positive 2 kV potential to a laser pulled spray tip at the end of the analytical column. The Velos-FTICR mass spectrometer was operated utilizing ReACT where ions with a charge state of four or greater were selected for high resolution MS^2 analysis in the ICR cell where an "on-the-fly" check of the observed fragment ion masses against the PIR mass relationship (Mass Precursor = Mass Reporter Ion + Mass Peptide 1 + Mass Peptide 2) is performed. Masses that satisfied the PIR relationship within a tolerance of 20 ppm mass error triggered subsequent low resolution MS^3 analyses of the released cross-linked peptide ions.

Parallel reaction monitoring (PRM) targeted analysis of selected cross-linked peptide pairs was performed using an Easy nLC 1000 system coupled with a Q-Exactive Plus mass spectrometer (Thermo Scientific). Samples containing cross-linked peptides were loaded onto a 3 cm × 100 μm trap column packed with 5 μm Reprosil C8 particles with 120 Å pores over a 10 min period using a flow rate of 2 μL/min of solvent A (H2O containing 0.1% formic acid). Peptides were separated by reversed-phase chromatography over a 60 cm × 75 μm analytical column packed with the same stationary phase as the trap column by applying

a linear gradient from 98% solvent A and 2% solvent B (acetonitrile containing 0.1% formic acid) to 60% solvent A and 40% solvent B over 120 minutes at a flow rate of 300 nL/min. Eluting peptides were ionized by electrospray ionization by applying a voltage of 2.2 kV to a laser pulled tip at the tip of the analytical column. The Q-Exactive Plus mass spectrometer was operated using a PRM method with the following settings: a single MS1 scan 150–2000 m/z at 70K resolving power with an AGC setting of 3E6 and a maximum ion accumulation time of 200 ms. Precursor ions for the targeted cross-linked peptide pairs were isolated with a 3.0 m/z window and fragmented by HCD using a normalized collision energy of 25. MS2 scans on the resulting fragment ions were performed at 17,500 resolving power with an AGC target value of 2E5 and a maximum ion accumulation time of 200 ms.

Generation of a Stage 1 Database of Putative Cross-linked Proteins—A sample of 1.0 mg of total cross-linked protein was generated by pooling 143 μg of protein from each of the PIR cross-linked HeLa cells that were treated various concentrations of PTX(0, 5, 10, 20, 50, 100, 500 nM). 100 μL of UltraLink monomeric avidin slurry was added to the pooled protein sample was and incubated at room temperature for 30 min. The monomeric avidin beads were washed 5 times with 1mL of 0.1 M NH_4HCO_3 pH 8.0 before eluting PIR reactive proteins using 100uL of 8M urea containing 2 mM biotin in 0.1 M NH_4HCO_3 pH 8.0. Disulfide bonds in the eluted proteins were reduced with 5 mM TCEP for 30 minutes followed by alkylation with 10 mM iodoacetamide for 45 minutes. Samples were diluted 10x with 0.1 M NH_4HCO_3 pH 8.0 before overnight digestion with a 1:200 ratio of trypsin at 37°C. The peptide samples were then desalted using C18 SepPak cartridges, followed by concentration and removal of acetonitrile by vacuum centrifugation using an EZ2-Plus evaporator.

The sample volume was adjusted to 100 μL with 0.1% formic acid before being analyzed by data dependent LC-MS/MS using an Easy-nLC (Thermo) coupled to a Q-Exactive Plus mass spectrometer (Thermo). Peptides were separated by reversed-phase chromatography using in-house packed C18 columns. Peptides were loaded onto a 3 cm × 100 μm inner diameter fused silica trap column packed with a stationary phase consisting of ReproSil C18, 5 μm diameter, 200 Å pore size particles (Dr. Maisch GmbH) with a flow rate of 2 μL/min of mobile phase consisting of 98% solvent A (H2O containing 0.1% formic acid) and 2% solvent B (ACN containing 0.1% formic acid) for 10 minutes. Peptides were then fractionated over a 60 cm × 75 μm inner diameter fused silica analytical column packed with ReproSil C18, 5 μm diameter, 100 Å pore size particles (Dr. Maisch GmbH) by applying a linear gradient from 90% solvent A, 10% solvent B to 60% solvent A, 40% solvent B over 120 minutes at a flow rate of 300 nL/min. Eluting peptide ions were ionized by nano-electrospray ionization by applying a positive 2 kV potential to a laser pulled spray tip at the end of the analytical column. The Q-Exactive Plus mass spectrometer operated using a data dependent analysis method consisting of a MS1 scan at 70,000 resolving power at m/z 200 followed by MS2 scans at 17,500 resolving power on the 20 most abundant ions in the MS1. Ions selected for MS2 were isolated using a 1.6 m/z isolation window, and fragmented by higher-energy collisional dissociation (HCD) using a normalized collision energy of 27. Additional MS2 settings included an automatic gain control (AGC) setting of 50,000 ions, a maximum ion accumulation time of 50 ms, charge state exclusion settings to not select ions

with charge states of one, more than eight or unassigned and a dynamic exclusion time of 30 s.

Mass spectral data acquired on the Q-Exactive plus was searched against the human UniProt database containing both forward and reverse protein sequences (downloaded 04/23/18, containing 40,632 total sequences) using Comet (version 2018.01 rev. 2) (Eng et al., 2013). Default parameters were used unless stated otherwise. The mass error tolerance was set to 20 ppm for the precursor mass allowing for standard 13C error offsets (−1/0/1/2/3). Carbamidomethylated cysteine was specified as a static modification while methionine oxidation and lysine acetylation were included as variable modifications. Resulting peptide spectrum matches were filtered analyzed by peptide and protein prophet and filtered at 1% FDR. A total of 29,458 non-redundant peptide sequences were identified corresponding to 3815 proteins. The stage 1 database used to search the ReACT generated MS3 spectra, as described below, consisted of the forward and reverse sequences of these 3185 proteins.

Quantification of relative protein abundance—Global protein abundance level analysis was performed using samples consisting of fractions 1–5 from the SCX separation, which contain the bulk of non-cross-linked peptides. Samples were desalted using C18 Sep-Pak cartridges (Waters). Desalted samples were concentrated by vacuum centrifugation using an EZ2-Plus evaporator. Peptide samples were adjusted to a concentration of 0.33 μg/μL with 0.1% formic acid and analyzed using the Easy-nLC/ Q-Exactive Plus system as described above.

Identification of cross-linked peptide pairs from MS spectra—Mass spectral data acquired on the Velos-FTICR was searched against the stage 1 database of putative cross-linked proteins which contained forward and reverse sequences for 3815 proteins (7630 total sequences) identified in the strategy described in the preceding section using Comet. Comet parameters included a 20 ppm precursor mass tolerance allowing for −1/0/1/2/3 ^{13}C offsets. Oxidation of Methionine (15.9949 Da) and acetylation of Lys (42.010565 Da) were included as variable modifications allowing for up to 3 instances of each modification per peptide sequence. Acetylation was not allowed to occur at C-terminal Lys residues. A single instance of Lys modified by the residual mass from the BDP cross-linker (197.032422 Da) was set to a required modification per peptide sequence to occur anywhere but the C-terminal Lys. Carbamidomethylation (57.021464 Da) was added to Cys as a static modification. For the heavy isotope SILAC search 8.014199 Da was added to Lys and 6.020129 Da was added to Arg as static modifications. Only fully tryptic peptide sequences with masses between 300 and 8000 Da were considered allowing for up to 5 missed cleavage sites. The mass tolerance for the fragment ions detected in the ion trap MS3 spectra was set to 1.0005 Da with a fragment bin offset of 0.4. The max precursor ion charge state was set to 6 and spectra were required to contain at least 10 peaks in order to be searched. The resulting pep.xml files from the Comet search were processed with XLinkProphet using default parameters (Keller et al., 2019a) to compute discriminating probabilities and filter the final dataset to less than 1% estimated false discovery rate (FDR) at the non-redundant cross-linked peptide pair level.

MS1 based quantification of SILAC labeled peptides—Quantification of the MS1 signal of the light and heavy SILAC isotope pairs for cross-linked peptides and non-cross-linked peptides was performed with MassChroQ v.2.1.1 (Valot et al., 2011). Data was loaded into MassChroQ in mzXML format with the corresponding peptide ID files containing the peptide sequence identification information in tab delimited text format. Peptide ID files contained five columns of data including the MS2 scan number where the identification was made, the stripped peptide sequence, the $[M+H]^+$ value for the light isotope form of the peptide, the charge state, the protein identifier and a mods column containing the peptide sequence with modification mass information. For each cross-liked peptide pair three $[M+H]^+$ values for light SILAC form were input corresponding to the most intense isotope of the precursor ion isotope envelope and the neighboring $\pm$ ^{13}C values calculated as described by Yergey (1983). Data from cross-linked peptide were grouped into five groups according to the SCX fractions collected (described above). Isotope label masses for SILAC heavy Arg (6.020129 Da) and Lys (8.014199 Da) were included. Retention time alignment was performed using the obiwarp method with a lmat precision setting of 1, a m/z start value of 500 and a m/z stop value of 1200. MS1 signal was extracted using a xic_extraction setting of max with a ppm range of $\pm$ 10 ppm. An anti spike filter setting of 5 was used. The Zivy peak detection algorithm was used with a mean_filter_half_edge setting of 1 and minmax_half_edge setting of 8 and maxmin_half_edge setting of 3. The detection threshold on max was set to 30000 and the detection threshold on min was set to 15000.

Measurement of mitochondrial bioenergetics and function—OCR (oxygen consumption rate) measurement was performed to using the XF^{e}24 Extracellular Flux analyzer (Seahorse Biosciences). HeLa cells, treated with different concentrations of PTX (0, 5, 10, 20, 500 nM) for 18 hours, were plated in growth medium at 5×10^4 cells/well the day before analysis. Prior to assay, cells were washed twice with the XF assay buffer (supplemented with 5.5 mM glucose, 1 mM sodium pyruvate and 4mM L-glutamine, pH 7.4). Then, cells were cultured in a non-CO$_2$ incubator for 30 min before assay. Following basal respiration measurements, cells were sequentially treated with 1 μM oligomycin A, 1 μM FCCP and 1 μM rotenone & antimycin A to record mitochondrial respiration. After the assay, cells were lysed with RIPA lysis buffer (50 μl/well) and protein concentration was determined. The OCR data was normalized to total protein amount and expressed as pmol/min/ug protein. Mitochondrial function parameters of basal respiration (difference in OCR before treatment of mitochondrial inhibitors and after rotenone & antimycin A treatment), ATP-dependent respiration (difference in OCR following oligomycin treatment and before any treatment), maximal respiration (difference in OCR following treatment of FCCP and rotenone & antimycin A) and proton leak respiration (difference in OCR following treatment of oligomycin and rotenone & antimycin A) were determined. All treatment conditions in the single assay were determined minimally in triplicate and three independent experiments were performed.

QUANTIFICATION AND STATISTICAL ANALYSIS

Integrated peak areas from the three most abundant isotopes for each cross-linked peptide pair resulting from MassChroQ v.2.1.1 (Valot et al., 2011) were used to calculate log2 based ratios (PTX/DMSO). Replicate log2 ratios were averaged across technical LC-MS replicates

(n = 3) and biological replicates (n = 2) to obtain mean values for each non-redundant cross-linked peptide pair at each drug treatment concentration (Table S1). Outlier ratios, defined by the interquartile range (IQR) test (values below Q1−1.5*IQR or above Q3+1.5*IQR) were removed prior to calculation of the mean. For ratios with replicate measurements 95% confidence intervals were calculated (Table S1). Relative protein abundances were calculated as the mean log2 ratios of their assigned non-cross-linked peptides, using the IQR test to remove outlier peptide log2 ratios (Table S2).

K-means clustering of quantified cross-linked peptide pairs—Longitudinal k-means clustering was performed with the R-package KML (Genolini et al., 2015). A set 1078 cross-linked peptide pairs that were quantified in at least three of the drug concentrations with 95% confidence intervals less than one were submitted for cluster analysis. Settings for KML included considering from 3–6 clusters allowing for 100 initialization events per cluster. The resulting clusters were evaluated using multiple criteria including three variants of Calinski Harabatz, Ray Turi, and Davies Bouldin. A result including three clusters, consisting of general trends of increasing, decreasing and non-changing was selected based on maximized normalized scores for 3 of the 5 criteria as well as the principle of Occam's Razor.

DATA AND CODE AVAILABILITY

The datasets generated during this study are available at XLinkDB http://xlinkdb.gs.washington.edu/xlinkdb/HeLa_PTX_titration_Bruce.php. The accession number for the LC-MS data reported in this paper is PRIDE: PXD015751.

Supplementary Material

Refer to Web version on PubMed Central for supplementary material.

REFERENCES

Adamska A, Domenichini A, and Falasca M (2017). Pancreatic Ductal Adenocarcinoma: Current and Evolving Therapies. Int. J. Mol. Sci 18, E1338. [PubMed: 28640192]

Afghani N, Mehta T, Wang J, Tang N, Skalli O, and Quick QA (2017). Microtubule actin cross-linking factor 1, a novel target in glioblastoma. Int. J. Oncol 50, 310–316. [PubMed: 27959385]

Albrethsen J, Angeletti RH, Horwitz SB, and Yang CP (2014). Proteomics ofcancercell lines resistant to microtubule-stabilizing agents. Mol. Can-cerTher 13, 260–269.

Alushin GM, Lander GC, Kellogg EH, Zhang R, Baker D, and Nogales E (2014). High-resolution microtubule structures reveal the structural transitions in αβ-tubulin upon GTP hydrolysis. Cell 157, 1117–1129. [PubMed: 24855948]

Ande SR, Xu YXZ, and Mishra S (2017). Prohibitin: a potential therapeutic target in tyrosine kinase signaling. Signal Transduct. Target. Ther 2, 17059. [PubMed: 29263933]

Bauman PA, Dalton WS, Anderson JM, and Cress AE (1994). Expression ofcytokeratin confers multiple drug resistance. Proc. Natl. Acad. Sci. USA 91, 5311–5314. [PubMed: 7515497]

Bavelloni A, Piazzi M, Raffini M, Faenza I, and Blalock WL (2015). Prohibitin 2: At a communications crossroads. IUBMB Life 67, 239–254. [PubMed: 25904163]

Becher I, Andrès-Pons A, Romanov N, Stein F, Schramm M, Baudin F, Helm D, Kurzawa N, Mateus A, Mackmull MT, et al. (2018). Pervasive Protein Thermal Stability Variation during the Cell Cycle. Cell 173,1495–1507. [PubMed: 29706546]

Bhasin MK, Ndebele K, Bucur O, Yee EU, Otu HH, Plati J, Bullock A, Gu X, Castan E, Zhang P, et al. (2016). Meta-analysis of transcriptome data identifies a novel5-gene pancreatic adenocarcinoma classifier. Oncotarget 7, 23263–23281. [PubMed: 26993610]

Bhatia S,Diedrich D,Frieg B,Ahlert H,Stein S,Bopp B,Lang F,Zang T, Kröger T, Ernst T, et al. (2018). Targeting HSP90 dimerization via the C terminus is effective in imatinib-resistant CML and lacks the heat shock response. Blood 732, 307–320.

Byrd CA, Bornmann W, Erdjument-Bromage H, Tempst P, Pavletich N, Rosen N, Nathan CF, and Ding A (1999). Heat shock protein 90 mediates macrophage activation by Taxol and bacterial lipopolysaccharide. Proc. Natl. Acad. Sci. USA 96, 5645–5650. [PubMed: 10318938]

Caulin C, Salvesen GS, and Oshima RG (1997). Caspase cleavage of keratin 18 and reorganization of intermediate filaments during epithelial cell apoptosis. J. Cell Biol 138, 1379–1394. [PubMed: 9298992]

Chavez JD, and Bruce JE (2019). Chemical cross-linking with mass spectrometry: a tool for systems structural biology. Curr. Opin. Chem. Biol 48, 8–18. [PubMed: 30172868]

Chavez JD, Weisbrod CR, Zheng C, Eng JK, and Bruce JE (2013). Protein interactions, post-translational modifications and topologies in human cells. Mol. Cell. Proteomics 12, 1451–1467. [PubMed: 23354917]

Chavez JD, Schweppe DK, Eng JK, Zheng C,Taipale A, Zhang Y, Ta-kara K, and Bruce JE (2015). Quantitative interactome analysis reveals a chemoresistant edgotype. Nat. Commun 6, 7928. [PubMed: 26235782]

Chavez JD, Eng JK, Schweppe DK, Cilia M, Rivera K, Zhong X, Wu X, Allen T, Khurgel M, Kumar A, et al. (2016a). A General Method forTar-geted Quantitative Cross-Linking Mass Spectrometry. PLoS ONE 11, e0167547. [PubMed: 27997545]

Chavez JD, Schweppe DK, Eng JK, and Bruce JE (2016b). *In Vivo* Conformational Dynamics of Hsp90 and lts lnteractors. Cell Chem. Biol 23, 716–726. [PubMed: 27341434]

Chavez JD, Lee CF, Caudal A, Keller A, Tian R, and Bruce JE (2018). Chemical Crosslinking Mass Spectrometry Analysis of Protein Conformations and Supercomplexes in Heart Tissue. Cell Syst. 6, 136–141. [PubMed: 29199018]

Chavez JD, Mohr JP, Mathay M, Zhong X, Keller A, and Bruce JE (2019). Systems structural biology measurements by *in vivo* cross-linking with mass spectrometry. Nat. Protoc 14, 2318–2343. [PubMed: 31270507]

Chen ZA, and Rappsilber J (2018). Protein Dynamics in Solution by Quantitative Crosslinking/Mass Spectrometry. Trends Biochem. Sci 43, 908–920. [PubMed: 30318267]

Csermely P, Schnaider T, Soti C, Prohászka Z, and Nardai G (1998). The 90-kDa molecular chaperone family: structure, function, and clinical applications. A comprehensive review. Pharmacol. Ther 79, 129–168. [PubMed: 9749880]

Datta S, Choudhury D, Das A, Das Mukherjee D, Das N, Roy SS, and Chakrabarti G (2017). Paclitaxel resistance development is associated with biphasic changes in reactive oxygen species, mitochondrial membrane potential and autophagy with elevated energy production capacity in lung cancer cells: A chronological study. Tumour Biol. 39, 1010428317694314.

Ding YH, Gong Z, Dong X, Liu K, Liu Z, Liu C, He SM, Dong MQ, and Tang C (2017). Modeling Protein Excited-state Structures from "Overlength" Chemical Cross-links. J. Biol. Chem 292, 1187–1196. [PubMed: 27994050]

Donnelly A, and Blagg BS (2008). Novobiocin and additional inhibitors of the Hsp90 C-terminal nucleotide-binding pocket. Curr. Med. Chem 15, 2702–2717. [PubMed: 18991631]

Echeverria PC, Bhattacharya K, Joshi A, Wang T, and Picard D (2019). The sensitivity to Hsp90 inhibitors of both normal and oncogenically transformed cells is determined by the equilibrium between cellular quiescence and activity. PLoS ONE 14, e0208287. [PubMed: 30726209]

Eng JK, Jahan TA, and Hoopmann MR (2013). Comet: an open-source MS/MS sequence database search tool. Proteomics 13, 22–24. [PubMed: 23148064]

Eskew JD, Sadikot T, Morales P, Duren A, Dunwiddie l., Swink M, Zhang X, Hembruff S, Donnelly A, Rajewski RA, et al. (2011). Development and characterization of a novel C-terminal inhibitor of Hsp90 in androgen dependent and independent prostate cancer cells. BMC Cancer 11, 468. [PubMed: 22039910]

Forry-Schaudies S, Murray JM, Toyama Y, and Holtzer H (1986). Effects of colcemid and taxol on microtubules and intermediate filaments in chick embryo fibroblasts. Cell Motil. Cytoskeleton 6, 324–338. [PubMed: 2874896]

Garrido-Laguna l., and Hidalgo M (2015). Pancreatic cancer: from state-of-the-art treatments to promising novel therapies. Nat. Rev. Clin. Oncol 12, 319–334. [PubMed: 25824606]

Genolini C, Alacoque X, Sentenac M, and Arnaud C (2015). kml and kml3d: R Packages to Cluster Longitudinal Data. J. Stat. Software 65, 1–34.

Goryunov D, and Liem RK (2016). Microtubule-Actin Cross-Linking Factor 1: Domains, lnteraction Partners, and Tissue-Specific Functions. Methods En-zymol. 569, 331–353.

Herman B, Langevin MA, and Albertini DF (1983). The effects of taxol on the organization ofthe cytoskeleton in cultured ovarian granulosa cells. Eur. J. Cell Biol 31, 34–45. [PubMed: 6137363]

Karantza V (2011). Keratins in health and cancer: more than mere epithelial cell markers. Oncogene 30, 127–138. [PubMed: 20890307]

Kavallaris M, Kuo DY, Burkhart CA, Regl DL, Norris MD, Haber M, and Horwitz SB (1997). Taxol-resistant epithelial ovarian tumors are associated with altered expression of specific beta-tubulin isotypes. J. Clin. lnvest 100, 1282–1293.

Keller A, Chavez JD, and Bruce JE (2019a). lncreased Sensitivity with Automated Validation of XL-MS Cleavable Peptide Crosslinks. Bioinformatics 35, 895–897. [PubMed: 30137231]

Keller A, Chavez JD, Eng JK, Thornton Z, and Bruce JE (2019b). Tools for 3D lnteractome Visualization. J. Proteome Res 18, 753–758. [PubMed: 30520642]

Klett H, Fuellgraf H, Levit-Zerdoun E, Hussung S, Kowar S, Kusters S, Bronsert P, Werner M, Wittel U, Fritsch R, et al. (2018). ldentification and Validation of a Diagnostic and Prognostic Multi-Gene Biomarker Panel for Pancreatic Ductal Adenocarcinoma. Front. Genet 9, 108. [PubMed: 29675033]

Komlodi-Pasztor E, Sackett D, Wilkerson J, and Fojo T (2011). Mitosis is not a key target of microtubule agents in patient tumors. Nat. Rev. Clin. Oncol 8, 244–250. [PubMed: 21283127]

Komuro A, Masuda Y, Kobayashi K, Babbitt R, Gunel M, Flavell RA, and Marchesi VT (2004). The AHNAKs are a class of giant propeller-like proteins that associate with calcium channel proteins of cardiomyocytes and other cells. Proc. Natl. Acad. Sci. USA 101, 4053–4058. [PubMed: 15007166]

Liberti MV, and Locasale JW (2016). The Warburg Effect: How Does it Benefit Cancer Cells? Trends Biochem. Sci 41, 211–218. [PubMed: 26778478]

Lopez J, and Tait SW (2015). Mitochondrial apoptosis: killing cancer using the enemy within. Br. J. Cancer 112, 957–962. [PubMed: 25742467]

Lu D, Wang J, Shi X, Yue B, and Hao J (2017). AHNAK2 is a potential prognostic biomarker in patients with PDAC. Oncotarget 8, 31775–31784. [PubMed: 28423668]

Maldonado EN, Patnaik J, Mullins MR, and Lemasters JJ (2010). Free tubulin modulates mitochondrial membrane potential in cancer cells. Cancer Res. 70, 10192–10201. [PubMed: 21159641]

Maldonado EN, DeHart DN, Patnaik J, Klatt SC, Gooz MB, and Lemasters JJ (2016). ATP/ADP Turnover and lmport of Glycolytic ATP into Mitochondria in Cancer Cells ls lndependent oftheAdenine NucleotideTrans-locator. J. Biol. Chem 291, 19642–19650. [PubMed: 27458020]

Miao Z, Ali A, Hu L, Zhao F, Yin C, Chen C, Yang T, and Qian A (2017). Microtubule actin cross-linking factor 1, a novel potential target in cancer. Cancer Sci. 108, 1953–1958. [PubMed: 28782898]

Mitchison TJ (2012). The proliferation rate paradox in antimitotic chemotherapy. Mol. Biol. Cell 23, 1–6. [PubMed: 22210845]

Neckers L, and Workman P (2012). Hsp90 molecular chaperone inhibitors: are we there yet? Clin. Cancer Res 18, 64–76. [PubMed: 22215907]

Nogales E, Wolf SG, and Downing KH (1998). Structure ofthe alpha beta tubulin dimer by electron crystallography. Nature 391, 199–203. [PubMed: 9428769]

Ong SE, Blagoev B, Kratchmarova l., Kristensen DB, Steen H, Pandey A, and Mann M (2002). Stable isotope labeling by amino acids in cell culture, SlLAC, as a simple and accurate approach to expression proteomics. Mol. Cell. Proteomics 1, 376–386. [PubMed: 12118079]

Oropesa M, de la Mata M, Maraver JG, Cordero MD, Cotán D, Rodrí-guez-Hernández A, Domínguez-Moñino I, de Miguel M, Navas P, and Sánchez-Alcázar JA (2011). Apoptotic microtubule network organization and maintenance depend on high cellular ATP levels and energized mitochondria. Apoptosis 76, 404–424.

Patel N, Chatterjee SK, Vrbanac V, Chung I, Mu CJ, Olsen RR, Wa-ghorne C, and Zetter BR (2010). Rescue of paclitaxel sensitivity by repression of Prohibitin1 in drug-resistant cancer cells. Proc. Natl. Acad. Sci. USA 707, 2503–2508.

Peng YT, Chen P, Ouyang RY, and Song L (2015). Multifaceted role of prohibitin in cell survival and apoptosis. Apoptosis 20, 1135–1149. [PubMed: 26091791]

Pfleger J, He M, and Abdellatif M (2015). Mitochondrial complex II is a source of the reserve respiratory capacity that is regulated by metabolic sensors and promotes cell survival. Cell Death Dis. 6, e1835. [PubMed: 26225774]

Pletjushkina OJ, Ivanova OJ, Kaverina IN, and Vasiliev JM (1994). Taxol-treated fibroblasts acquire an epithelioid shape and a circular pattern of actin bundles. Exp. Cell Res 272, 201–208.

Polier G, Neumann J, Thuaud F, Ribeiro N, Gelhaus C, Schmidt H, Giaisi M, Köhler R, Müller WW, Proksch P, et al. (2012). The natural anticancer compounds rocaglamides inhibit the Raf-MEK-ERK pathway by targeting prohibitin 1 and 2. Chem. Biol 79, 1093–1104.

Quick QA (2018). Microtubule-Actin Crosslinking Factor 1 and Plakins as Therapeutic Drug Targets. Int. J. Mol. Sci 79, E368.

Rosenblum MD, and Shivers RR (2000). 'Rings' of F-actin form around the nucleus in cultured human MCF7 adenocarcinoma cells upon exposure to both taxol and taxotere. Comp. Biochem. Physiol. C Toxicol. Pharmacol 725,121–131.

Sarhan AR, Patel TR, Cowell AR, Tomlinson MG, Hellberg C, Heath JK, Cunningham DL, and Hotchin NA (2016). LAR proteintyrosine phosphatase regulatesfocal adhesionsthrough CDK1. J. Cell Sci 729,2962–2971.

Sarosiek KA, Ni Chonghaile T, and Letai A (2013). Mitochondria: gatekeepers of response to chemotherapy. Trends Cell Biol. 23, 612–619. [PubMed: 24060597]

Schweppe DK, Zheng C, Chavez JD, Navare AT, Wu X, Eng JK, and Bruce JE (2016). XLinkDB 2.0: integrated, large-scale structural analysis of protein crosslinking data. Bioinformatics 32, 2716–2718. [PubMed: 27153666]

Solit DB, Basso AD, Olshen AB, Scher HI, and Rosen N (2003). Inhibition of heat shock protein 90 function down-regulates Akt kinase and sensitizes tumors to Taxol. Cancer Res. 63, 2139–2144. [PubMed: 12727831]

Soulieres D, Hirsch FR, Shepherd FA, Bordogna W, Delmar P, Shames DS, and Klughammer B (2015). PTPRF Expression as a Potential Prognostic/Predictive Marker for Treatment with Erlotinib in Non-Small-Cell Lung Cancer. J. Thorac. Oncol 70, 1364–1369.

St-Denis N, Gupta GD, Lin ZY, Gonzalez-Badillo B, Veri AO, Knight JDR, Rajendran D, Couzens AL, Currie KW, Tkach JM, et al. (2016). Phenotypic and Interaction Profiling of the Human Phosphatases Identifies Diverse Mitotic Regulators. Cell Rep. 77, 2488–2501.

Tatsuta T, Model K, and Langer T (2005). Formation of membrane-bound ring complexes by prohibitins in mitochondria. Mol. Biol. Cell 76, 248–259.

Teh JT, Zhu WL, Newgard CB, Casey PJ, and Wang M (2019). Respi-ratoryCapacity and Reserve Predict Cell Sensitivityto Mitochondria Inhibitors: Mechanism-Based Markers to Identify Metformin-Responsive Cancers. Mol. Cancer Ther 78, 693–705.

Trendowski M (2014). Exploiting the cytoskeletal filaments of neoplastic cells to potentiate a novel therapeutic approach. Biochim. Biophys. Acta 7846, 599–616.

Trepel J, Mollapour M, Giaccone G, and Neckers L (2010). Targeting the dynamic HSP90 complex in cancer. Nat. Rev. Cancer 70, 537–549.

Um JW, and Ko J (2013). LAR-RPTPs: synaptic adhesion molecules that shape synapse development. Trends Cell Biol. 23, 465–475. [PubMed: 23916315]

Valot B, Langella O, Nano E, and Zivy M (2011). MassChroQ: a versatile tool for mass spectrometry quantification. Proteomics 77, 3572–3577.

Varbiro G, Veres B, Gallyas F Jr., and Sumegi B (2001). Direct effect of Taxol on free radical formation and mitochondrial permeability transition. Free Radic. Biol. Med 37, 548–558.

Vemu A, Atherton J, Spector JO, Moores CA, and Roll-Mecak A (2017). Tubulin isoform composition tunes microtubule dynamics. Mol. Biol. Cell 28, 3564–3572. [PubMed: 29021343]

Verba KA, Wang RY, Arakawa A, Liu Y, Shirouzu M, Yokoyama S, and Agard DA (2016). Atomic structure of Hsp90-C Ψ37-Cdk4 reveals that Hsp90 traps and stabilizes an unfolded kinase. Science 352, 1542–1547. [PubMed: 27339980]

Wang M, Li X, Zhang J, Yang Q, Chen W, Jin W, Huang YR, Yang R, and Gao WQ (2017). AHNAK2 is a Novel Prognostic Marker and Oncogenic Protein for Clear Cell Renal Cell Carcinoma. Theranostics 7, 1100–1113. [PubMed: 28435451]

Weaver BA (2014). HowTaxol/paclitaxel kills cancer cells. Mol. Biol. Cell 25, 2677–2681. [PubMed: 25213191]

Weisbrod CR, Chavez JD, Eng JK, Yang L, Zheng C, and Bruce JE (2013a). *In vivo* protein interaction network identified with a novel real-time cross-linked peptide identification strategy. J. Proteome Res 72,1569–1579.

Weisbrod CR, Hoopmann MR, Senko MW, and Bruce JE (2013b). Performance evaluation of a dual linear ion trap-Fourier transform ion cyclotron resonance mass spectrometer for proteomics research. J. Proteomics 88, 109–119. [PubMed: 23590889]

Winter A, Kämäräinen O, and Hofmann A (2007). Molecular modeling of prohibitin domains. Proteins 68, 353–362. [PubMed: 17427253]

Xu Y, and Fisher GJ (2012). Receptor type protein tyrosine phosphatases (RPTPs)-roles in signal transduction and human disease. J. Cell Commun. Signal 6, 125–138. [PubMed: 22851429]

Yang L, Zheng C, Weisbrod CR, Tang X, Munske GR, Hoopmann MR, Eng JK, and Bruce JE (2012). *In vivo* application of photocleavable protein interaction reporter technology. J. Proteome Res 77, 1027–1041.

Yergey JA (1983).Ageneral approach to calculating isotopic distributionsfor mass spectrometry. Int. J. Mass Spectrom. Ion Phys 52, 337–349.

Zasadil LM, Andersen KA, Yeum D, Rocque GB, Wilke LG, Tevaar-werk AJ, Raines RT, Burkard ME, and Weaver BA (2014). Cytotoxicity of paclitaxel in breast cancer is due to chromosome missegregation on multipolar spindles. Sci. Transl. Med 6, 229ra43.

Zhang H, Tang X, Munske GR, Zakharova N, Yang L, Zheng C, Wolff MA, Tolic N, Anderson GA, Shi L, et al. (2008). *In vivo* identification ofthe outer membrane protein OmcA-MtrC interaction network in *Shewanella oneidensis* MR-1 cells using novel hydrophobic chemical cross-linkers. J. Proteome Res 7, 1712–1720. [PubMed: 18303833]

Zheng C, Yang L, Hoopmann MR, Eng JK, Tang X, Weisbrod CR, and Bruce JE (2011). Cross-linking measurements of in vivo protein complex topologies. Mol. Cell. Proteomics 70, M110.006841.

Zheng C, Weisbrod CR, Chavez JD, Eng JK, Sharma V, Wu X, and Bruce JE (2013).XLink-DB: databaseand softwaretoolsforstoringandvisu-alizing protein interaction topology data. J. Proteome Res 72, 1989–1995.

Zhong X, Navare AT, Chavez JD, Eng JK, Schweppe DK, and Bruce JE (2017). Large-Scale and Targeted Quantitative Cross-Linking MS Using Isotope-Labeled Protein Interaction Reporter (PIR) Cross-Linkers. J. Proteome Res 76, 720–727.

Highlights

- Quantitative cross-linking/mass spectrometry analysis of mitotic inhibitor-treated cells

- Cross-links reflect paclitaxel stabilization of microtubules

- Drug-specific changes to intermediate and microfilament structures

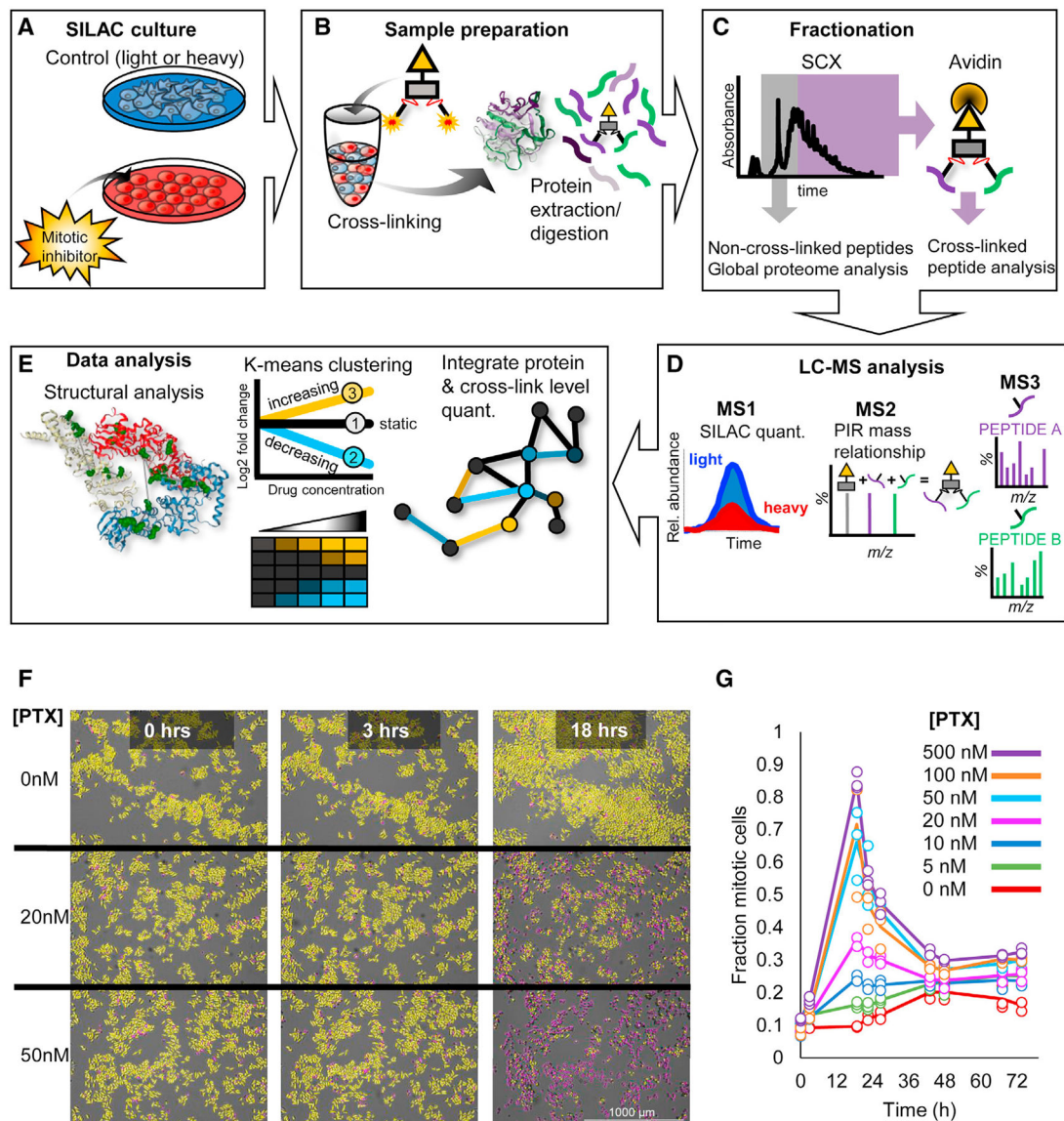- Paclitaxel treatment alters mitochondrial respiration and ATP synthase structure

Figure 1. Experimental Overview

(A) Cells are cultured in SILAC media; the isotopically light or heavy cells are treated with the mitotic inhibitors PTX (5, 10, 20, 50, 100, and 500 nM), NOC (3 μM), CA4 (5 nM), and STLC (5 μM); and the corresponding isotope pair is treated with 0.1% (v/v) DMSO vehicle control.

(B) Cells are cross-linked with 10 mM BDP-NHP, followed by lysis and protein extraction with 8 M urea and tryptic digestion.

(C) Peptide samples are fractionated by strong cation exchange (SCX) chromatography, with early eluting fractions (1–5) containing non-cross-linked peptides used for global proteome quantification and later fractions(6–14) subjected to avidin affinity chromatography and used for cross-linked peptide pair identification and quantification.

(D) LC-MS analysis consists of MS1 measurement of light and heavy SILAC isotope precursor ions followed by MS2 analysis of fragment ions. For cross-linked peptide pairs,

detection of a protein interaction reporter (PIR) mass relationship triggers MS3 of the released peptides for sequence determination.

(E) Data analysis consists of integrating protein-level and cross-link-level quantitative information. Drug concentration-dependent trends in cross-linked peptide pairs are identified by statistical filtering and longitudinal k-means clustering. Cross-link data are analyzed in terms of protein structural information.

(F) A collection of nine representative images of HeLa cells treated with PTX. PTX concentration increases (0, 20, and 50 nM) while scanning the images from the top to bottom, and treatment time increases(0, 3, and 18 h) from left to right. The cells are colored yellow by a software-applied mask, while rounded cells that are locked in mitosis are colored magenta. Scale bar of 1000 μm indicated on lower right image.

(G) Line graph plotting the fraction of mitotic cells on the y axis and PTX treatment time on the x axis (biological replicates, n = 3).

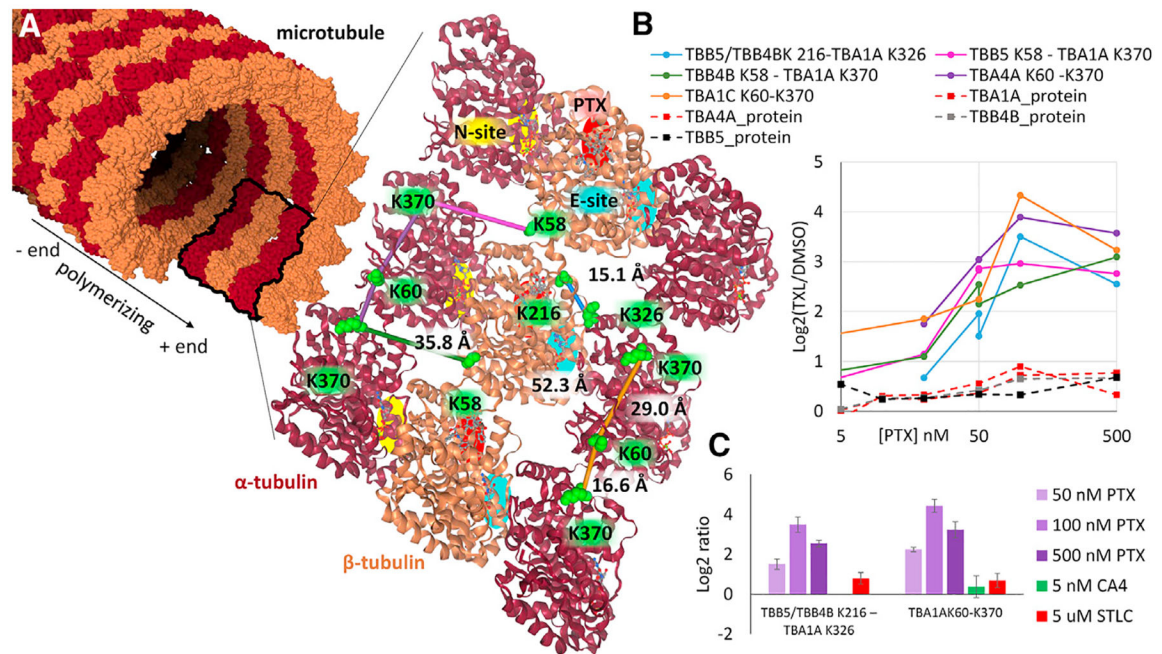**Figure 2. Quantitative Cross-Linking Reveals PTX Stabilized MTs**

(A) MT structure (PDB: 3EDL) displayed as a molecular surface with a ribbon structure inset, illustrating the α-tubulin (maroon) and β-tubulin (gold) subunits. Cross-linked Lys residues are shown as green space-filled residues, with cross-links displayed as colored bars connecting them (TBA1A K60-K370, orange; TBA4A K60-K370, purple; TBB5/TBB4B K216-TBA1A K326, blue; TBB4B K58-TBA1A K370, green; TBB5 K58-TBA1A K370, magenta). The non-exchangeable GTP binding site (N-site) is indicated by a yellow-highlighted region on α-tubulin. The exchangeable GTP binding site (E-site) is indicated by a cyan-colored region on β-tubulin. The PTX binding site on β-tubulin is red.

(B) Protein and cross-link levels measured by SILAC for four tubulin isoforms (TBA1A, dark red dashed line; TBA4A, red dashed line; TBB4B, gray dashed line; TBB5, black dashed line). Cross-links are colored the same as in (A).

(C) Quantified levels of TBB5/TBB4B K216-TBA1A K326 and TBA1A K60-K370 with PTX (50, 100, and 500 nM), CA4 (5 nM), and STLC (5 μM). Error bars represent 95% confidence intervals for n = 6 replicate injections of 2 biological samples.
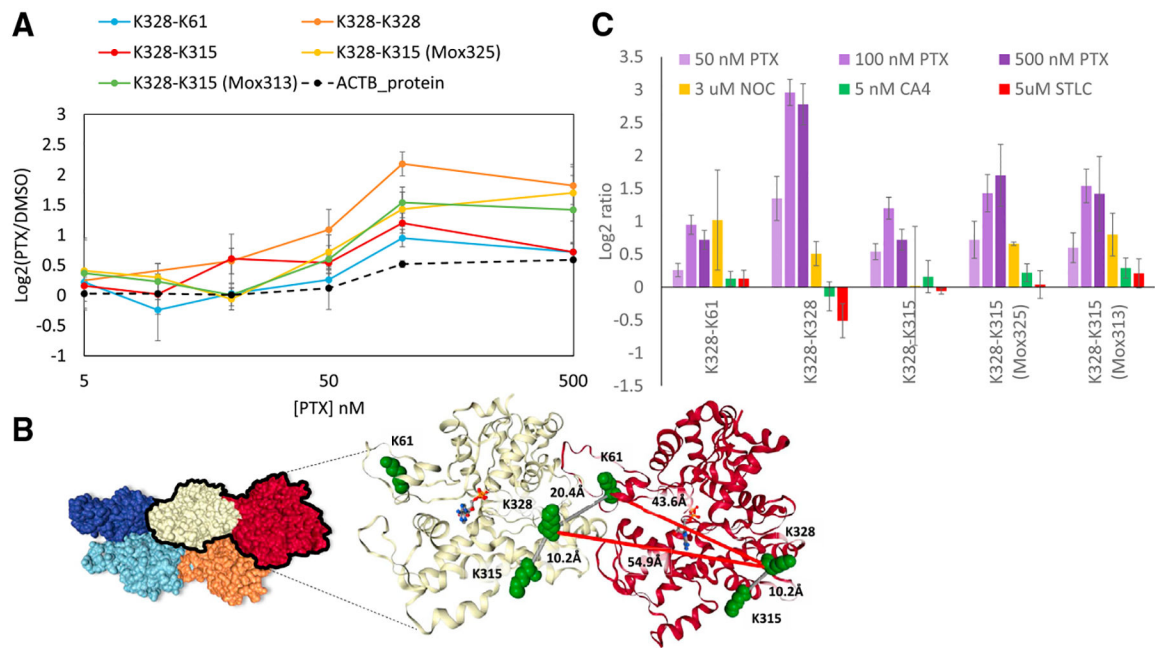
Figure 3. PTX Induced Effects on MFs

(A) Quantitation of cross-linked peptide pairs involving K328 of ACTB. Although the primary sequences for these peptide pairs were the same (IK330IIAPPER-MQK317EITALAPSTMK), one form contained only the cross-link modification on K328 and K317 (red line), while two other forms contained oxidation of methionine at M325 (yellow line) or M313 (green line). The ACTA protein level is shown as a black dashed line. Error bars represent 95% confidence intervals.

(B) MF structure (PDB: 6FHL) displayed as a molecular surface with five actin monomers and ribbon structures for two of the actin subunits. Cross-linked sites are displayed as green space-filled residues with the Cα-Cα distance displayed. The link between K328 and K315 is compatible with formation within a single actin subunit. The link between K328 and K61 exceeds the expected maximum cross-linkable distance (42 Å) when mapped within a single actin subunit but is compatible between neighboring actin subunits (20.4 Å). The homodimeric link at K328 is not compatible with forming between actin subunits existing with the structure of a single MF (54.9 Å) and therefore likely represents a different conformation. The K330 homodimer link could potentially form between actin subunits in neighboring MFs, where they come into close proximity, such as when they are packed into MF bundles.

(C) Bar chart illustrated quantified cross-linked peptide pair levels in actin with PTX (50, 100, and 500 nM), NOC (3 μM), CA4 (5 nM), and STLC (5 μM). Error bars represent 95% confidence intervals for n = 6 replicate injections of 2 biological samples.
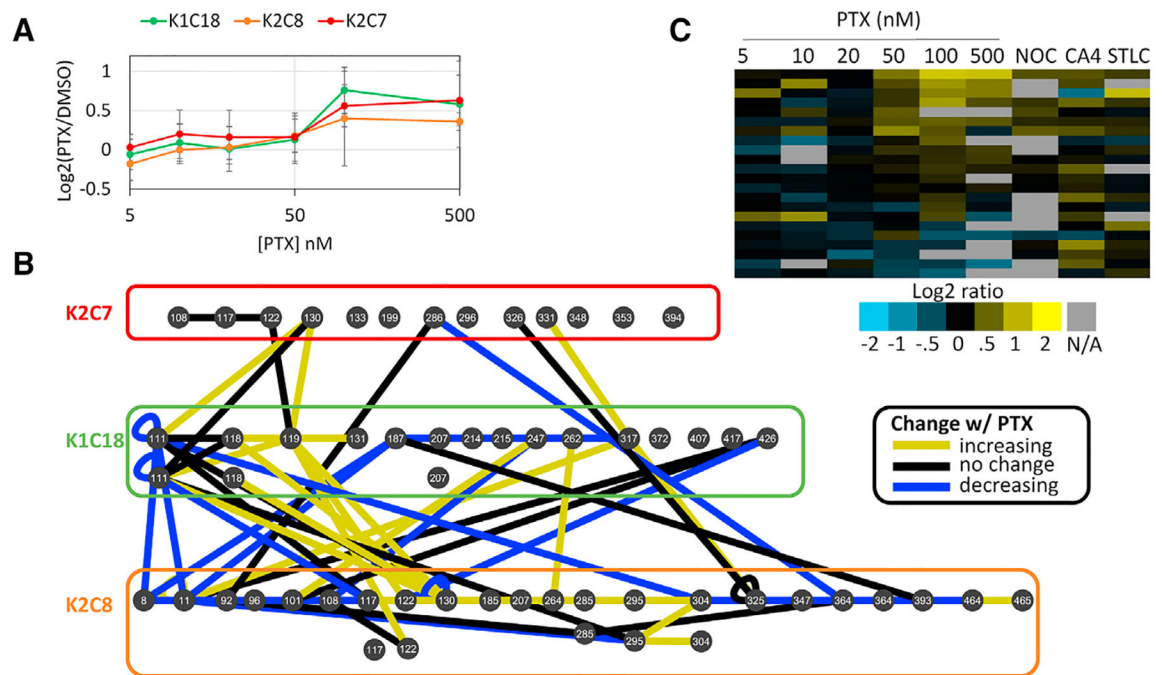
Figure 4. PTX Induced Effects on Keratin IFs

(A) Quantified protein abundances for three keratin isoforms (K1C18, green; K2C8, orange; K2C7, red). Error bars represent 95% confidence intervals from n = 6 replicate injections of 2 biological samples.

(B) Interaction network illustrating cross-linked Lys residues as nodes and cross-links as edges between and within K2C7 (red), K1C18 (green), and K2C8 (orange). Edges are colored according to KML cluster (Figure S2).

(C) Heatmap of 22 cross-links involving K2C8, K1C18, and K2C7 quantified with PTX concentrations ranging from 5–500 nM, NOC (3 μM), CA4 (5 nM), and STLC (5 μM). Values are mean log2 ratios from n = 6 replicate injections of 2 biological samples.
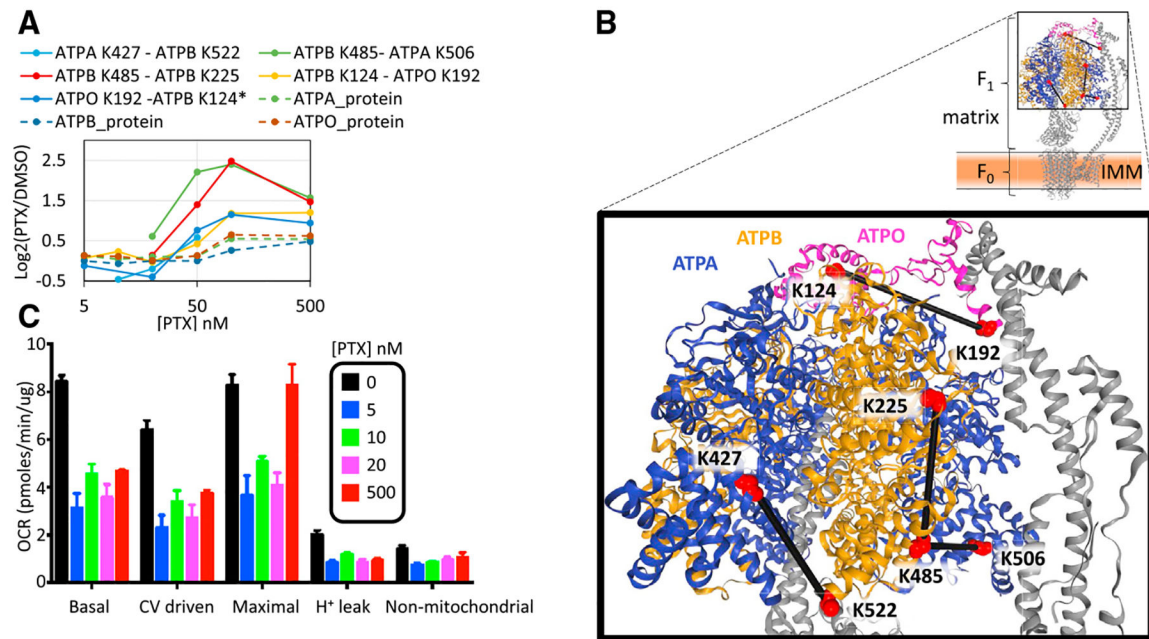
Figure 5. PTX Induced Conformational Change in CV

(A) Line graph illustrating relative cross-linked peptide pair and global protein abundance levels displayed as log2(PTX/DMSO) values on the y axis and PTX concentration on the x axis for CV subunits. Plotted cross-links are as follows: ATPA K427-ATPB K522 (light blue), ATPB K485-ATPA K506 (green), ATPB K485-K225 (orange), ATPB K124-ATPO K192 (yellow), ATPO K192-ATPB K124 (* indicates missed tryptic cleavage on the ATPB peptide GQKVLDSGAPIK^{124}IPVGPETLGR, dark blue), ATPA protein levels (green dashed line), ATPB protein levels (dark blue dashed line), and ATPO protein levels (brown dashed line).

(B) Ribbon structure of CV (PDB: 5ARA) illustrating the F$_1$ region, which extends into the mitochondrial matrix, and the F0 region, embedded in the inner-mitochondrial membrane. The zoomed inset illustrates ATPA (dark blue), ATPB (gold), and ATPO (magenta), with cross-linked Lys shown as red space-filled residues.

(C) Summary of mitochondrial oxygen consumption rate (OCR) measurements of HeLa cells treated with PTX (0, 5, 10, 20, and 500 nM) for 18 h. Data are represented as mean ± SEM with n = 9 (3 wells each for 3 replicate plates). See Figure S7F.
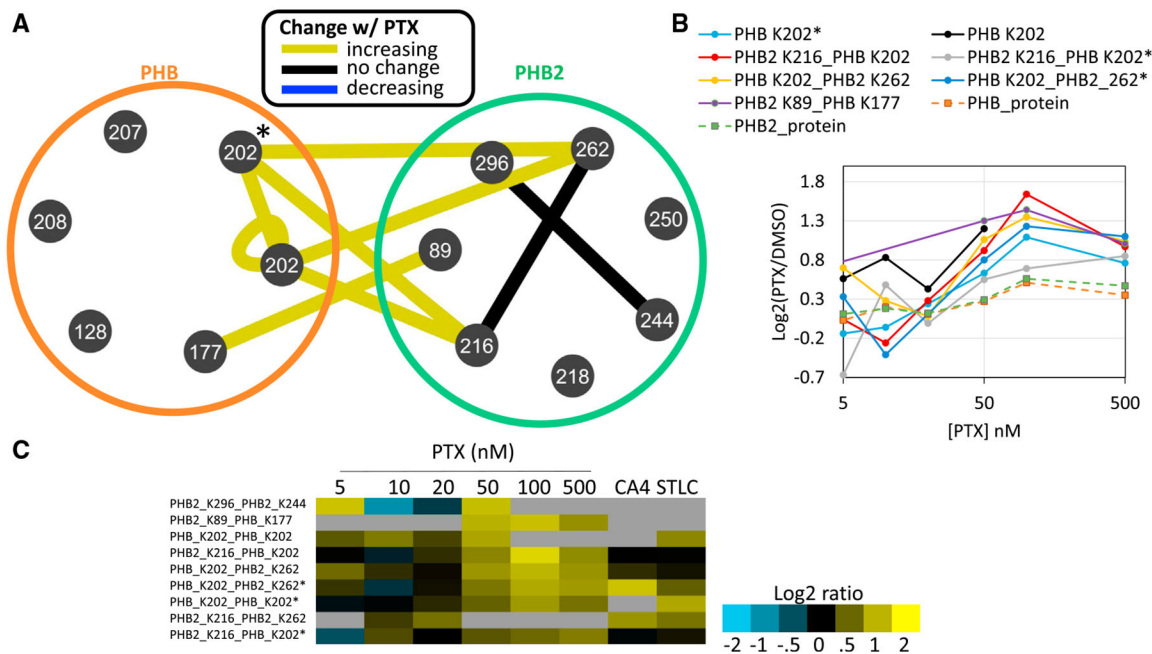
Figure 6. PTX Induced Changes to PHB Complex

(A) Interaction network of PHB (green) and PHB2 (orange) cross-links. Edges are colored according to KML cluster (Figure S2).

(B) Quantified protein and cross-link levels for PHBs: PHB (green dashed line), PHB2 (orange dashed line), PHB K202 (* indicates missed tryptic cleavage site on PHB peptide FVVEK^{202}AEQQKK homodimeric link, light blue), PHB K202 homodimeric link (black), PHB2 K216-PHB K202 (orange), PHB K216-PHB K202* (gray), PHB K202-PHB K262 (yellow), PHB K202-PHB2 K262 * (dark blue), and PHB2 K89-PHB K177 (green).

(C) Heatmap displaying quantified levels of 9 cross-links involving PHB and PHB2 from cells treated with PTX (5–500 nM), CA4 (5 nM), and STLC (5 μM). Values are mean log2 ratios from n = 6 replicate injections of 2 biological samples.
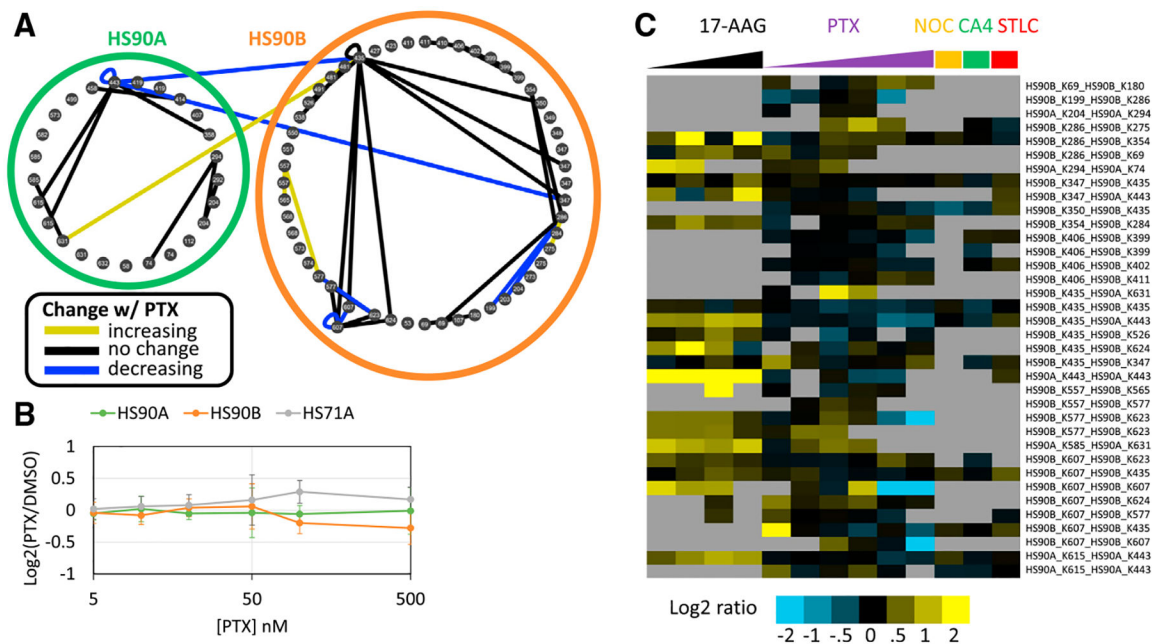
Figure 7. PTX Induced Changes to Hsp90

(A) Interaction network for HS90A (green) and HS90B (orange) cross-links. Edges are colored according to KML cluster (Figure S2).

(B) Quantified protein abundances of HS90A (green), HS90B (orange), and Hsp71-α (HS71A, gray) versus PTX concentration (x axis). Error bars represent 95% confidence intervals from n = 6 replicate injections of 2 biological samples.

(C) Heatmap of cross-links quantified from cells treated with 17-AAG, PTX, NOC, CA4, and STLC. The concentration of each drug increases from left to right. Values are mean log2 ratios from n = 6 replicate injections of 2 biological samples.

KEY RESOURCES TABLE

REAGENT or RESOURCE	SOURCE	IDENTIFIER
Chemicals, Peptides, and Recombinant Proteins		
BDP peptide for cross-linker. Sequence: Suc-Asp-Pro-Lys-(Pro-Asp-Suc)-Lys(biotin)-Gly on Clt resin	AnaSpec	Cat# 66727–2
Paclitaxel	Fisher Scientific	Cat# AC328420250
S-Trityl-L-cysteine	Millipore Sigma	Cat# 164739
Nocodazole	Millipore Sigma	Cat# M1404
Combretastatin A4	Millipore Sigma	Cat# C7744
Seahorse XF Base Medium	Agilent	Cat# 102353–100
Monomeric avidin UltraLink resin	ThermoFisher Scientific	Cat# 53146
Deposited Data		
Cross-link data deposited into XLinkDB	http://xlinkdb.gs.washington.edu/	Network Name: HeLa_PTX_titration_Bruce
LC-MS data deposited into PRIDE	https://www.ebi.ac.uk/pride/archive/	PRIDE: PXD015751
Experimental Models: Cell Lines		
HeLa cell line	ATCC	Cat# CCL-2, RRID:CVCL_0030
Software and Algorithms		
Comet v. 2018.01 rev. 2	Eng et al.,2013	http://comet-ms.sourceforge.net/
XLinkProphet	Keller et al., 2019a	https://github.com/brucelab/xlinkprophet
MassChroQ v.2.1.1	Valot et al., 2011	http://pappso.inra.fr/bioinfo/masschroq/